Phosphorylation Toggles the SARS-CoV-2 Nucleocapsid Protein Between Two Membrane-Associated Condensate States

Bruna Favetta[1], Huan Wang[2], Jasmine Cubuk[3], Mayur Barai[4], Cesar Ramirez[1], Adam J. Gormley[1], Sanjeeva Murthy[2], Andrea Soranno[3], Zheng Shi[2], Benjamin S. Schuster[4]

1 Department of Biomedical Engineering, Rutgers, The State University of New Jersey, Piscataway, NJ 08854
2 Department of Chemistry and Chemical Biology, Rutgers, The State University of New Jersey, Piscataway, NJ 08854
3 Department of Biochemistry and Molecular Biophysics, Washington University in St Louis, St. Louis, MO 63110
4 Department of Chemical and Biochemical Engineering, Rutgers, The State University of New Jersey, Piscataway, NJ 08854

Corresponding author benjamin.schuster@rutgers.edu

Key Words: SARS-CoV-2, liquid-liquid phase separation (LLPS), phosphorylation, protein-RNA interactions, material properties, membrane interaction

Summary

The SARS-CoV-2 Nucleocapsid protein (N) performs several functions during the viral lifecycle, including transcription regulation and viral genome encapsulation. We hypothesized that N toggles between these functions via phosphorylation-induced conformational change, thereby altering N interactions with membranes and RNA. We found that phosphorylation changes how biomolecular condensates composed of N and RNA interact with membranes: phosphorylated N (pN) condensates form thin films, while condensates with unmodified N are engulfed. This partly results from changes in material properties, with pN forming less viscous and elastic condensates. The weakening of protein-RNA interaction in condensates upon phosphorylation is driven by a decrease in binding between pN and unstructured RNA. We show that phosphorylation induces a conformational change in the serine/arginine-rich region of N that increases interaction between pN monomers and decreases nonspecific interaction with RNA. These findings connect the conformation, material properties, and membrane-associated states of N, with potential implications for COVID-19 treatment.

Introduction

The COVID pandemic has focused attention on the mechanisms of SARS-CoV-2 viral replication. SARS-CoV-2 is an enveloped virus with a non-segmented, positive-sense, single-stranded, ~30 kb RNA genome[1]. In the virus core, genomic RNA (gRNA) is associated with Nucleocapsid protein (N), forming a ribonucleoprotein (RNP) complex. N has several functions during the viral life cycle but is primarily involved in protecting the viral RNA genome by binding, condensing, and packaging it within the virion[2]. N has also been shown to be necessary for efficient transcription and replication of viral RNA, and it additionally contributes to immune evasion via sequestering stress granule proteins[3]. How N is regulated throughout the viral lifecycle to perform its varied functions, and whether it is possible to therapeutically manipulate this regulation to inhibit viral replication, remains unknown.

N is a multi-domain protein, consisting of two folded and three disordered domains (Figure 1A), the diversity of which likely contributes to its ability to perform several functions throughout the viral lifecycle[2]. The N-terminal folded domain (NTD) strongly binds with specific viral RNA elements, stabilizing

the RNP complex[4,5]. The C-terminal folded domain (CTD) mediates dimerization of N, facilitating the formation of the helical nucleocapsid structure that protects the viral RNA genome[6,7]. Both folded domains are flanked by disordered regions. The central disordered region acts as a linker that allows for conformational flexibility[8]. More specifically, the serine/arginine(SR)-rich region (aa 175 – 206; Figure 1B) within the linker is known to participate in both protein–protein and protein–RNA interactions[9–11].

Importantly, this SR-rich region was identified as a site of phosphorylation of N (Figure 1B) that may regulate its function, based on several lines of evidence. 1) At different stages of the viral life cycle, N exists in two phosphorylation states. Abundant phosphorylated protein is found inside infected cells, while unmodified protein is found within virions[12–16]. Regulation of phosphorylation of N may act as a timer in the viral lifecycle, switching from replication, transcription, and translation to assembly of new virions[17]. 2) Phosphorylation of the SR-rich region of N has been shown to modify how the protein interacts with RNA, as well as affect the transcription and translation of RNA[18,19]. 3) During viral replication, when N is likely phosphorylated, it was shown to form a thin layer around viral replication organelles (vROs), double membrane vesicles filled with viral RNA commonly found in infected cells[15,20]. However, during virion assembly, complexes of unmodified N and RNA remain as small, spherical structures while the viral capsid is engulfed by the ER-Golgi intermediate complex (ERGIC) membrane[21]. These observations suggest that phosphorylation of N and its membrane interactions are linked and may underlie N's multiple functions. The goal of this paper is to elucidate this link between N phosphorylation and its membrane interaction at the molecular level, providing insights critical for understanding COVID infection.

We sought to understand the phosphorylation-dependent membrane interactions of N through the lens of phase separation. N contains RNA-binding and disordered domains, which enable N and RNA to interact in a dynamic manner. This results in the formation of droplets enriched in protein and RNA, known as biomolecular condensates[3,8,22]. N undergoes phase separation with RNA in vitro and in vivo; experiments show that phosphorylation of N[17,22], type of RNA[23,24], and temperature[23] modulate the condensate's propensity to phase separate and affect its molecular dynamics. Biomolecular condensates can display a range of material properties, from liquids to gels, which may be closely associated with their function[25,26]. The material properties of a condensate need not be static, and cellular regulation can modulate its properties and thus its function[27]. Carlson et al. showed that unmodified N and RNA forms

gel-like condensates and discrete 15-nm particles, while phosphorylated N generates a more liquid-like droplet. They hypothesized that this difference in material properties could be the basis for a dual role of N during the viral lifecycle in both regulating RNA transcription and facilitating nucleocapsid assembly[28,29]. However, how the phosphorylation-dependent material properties of N condensates affect their interaction with membranes has not been studied. Recent investigations on condensate-membrane interaction support that condensate material properties are a key factor determining the mode of interaction between the liquid-like droplets and the membrane surface[30–32]. Based on this, we hypothesized that phosphorylation tunes how N and RNA interact, thus modulating the material properties of N and RNA condensates, consequently influencing condensate-membrane interaction, and in turn allowing N to display the two distinct behaviors observed throughout the viral life cycle (Figure 1C-D).

Here, we mapped how condensates composed of N and viral RNA fragments interact with membranes. We found the interaction depends on whether N is phosphorylated, as well as whether viral membrane proteins are present. We explained these membrane interactions in two ways. First, we examined how N vs. pN bind to membrane proteins, finding that phosphorylation inhibits interaction between N and the SARS-CoV-2 Membrane protein (M). Second, since we observed different degrees of remodeling of condensates around membranes, we hypothesized that the material properties of condensates also regulate membrane interaction. We found that N's phosphorylation status drastically alters condensate viscoelasticity, as does RNA type. Next, we investigated the molecular basis for these changes in condensate rheology. We found that phosphorylation and RNA structure affect N's ability to bind to RNA. We compared the structures of N and pN, revealing that phosphorylation causes increased interaction between pN monomers within dimers. We integrated these experimental results into a model that explains how phosphorylation alters the structure of N, consequently affecting its interaction with RNA, its dynamics within condensates, and its ability to interact with viral membrane proteins and membrane surfaces. We speculate that this change in the form of N condensates acts as a functional switch during the viral lifecycle, toggling N from roles in RNA replication to new virion assembly.

Results

We reconstituted N or pN and RNA condensates in vitro. We prepared recombinantly expressed N that was either kept unmodified or was phosphorylated in vitro using GSK-3β and SRPK1 kinases[16] (Figure 1B). An average of 9 phosphorylation sites on N was confirmed using mass spectrometry and Phos-Tag SDS-PAGE (Supplemental Figure 1). We used in vitro transcription to make fragments of viral RNA that are known to promote phase separation of N (Figure 1E)[23]. First, we tested a fragment containing the first 1000 base pairs from the 5' end of the viral genome that contains important regulatory information[1]. Second, we tested the fragment of RNA that encodes N (containing the first 75 nucleotides of the 5′ untranslated region recombined onto the N protein coding sequence), given it is highly produced during viral infection[1]. As expected, mixing N or pN protein with either RNA at 37°C resulted in their condensation into protein- and RNA-rich droplets (Figure 1F). A change in morphology with regards to the degree of sphericity of droplets already suggests that condensates are modulated by both type of RNA and phosphorylation status of the protein (Supplemental Figure 2), two factors that we investigate in depth.

N condensate composition determines interaction with membranes

Prior work has shown that following viral infection, N accumulates in thin layers around folded ER membranes that are likely vROs[33]. In contrast, later during viral budding events, N is part of RNPs linked by the viral genome[21]. These RNPs do not fuse or grow during the budding process, instead remaining as distinct complexes as the nucleocapsid is engulfed into new virions[21,34]. We first asked whether we could reproduce these two behaviors of N in vitro.

We developed a system to study the interaction between N and RNA condensates and membranes. We modeled membranes using giant unilamellar vesicles (GUVs). GUVs were made with a lipid composition meant to approximate the human ER membrane[35,36], with 60% DOPC, 25% DOPE, 10% DOPS, and the addition of 5% Ni-NTA lipids. The Ni-NTA lipids allowed us to tether membrane protein fragments to the GUV surface[37] to investigate whether the presence of either of two viral membrane proteins would affect condensate-GUV interaction (Figure 2A). The viral non-structural protein 3 (Nsp3) localizes to vROs[38] and was suggested to both help form the double layer of membranes as well as form

pores that span the membranes[39–41]. Nsp3 is a known interactor of N[42,43] and therefore is a logical candidate for modulating N's interaction with the membranes enveloping vROs. We also studied the viral M protein that is present in the ERGIC membrane where new virions form[44]. M and N are also known interactors, where M is thought to anchor the RNP complex to the membrane during new virion formation[45,46]. Given the challenges of producing and inserting transmembrane proteins into vesicles, we chose to study the domains of the proteins that are known to interact with N. For M, we used a construct with the C-terminal endodomain of the M protein, fused to a 6xHis tag and GFP[46]. For Nsp3, we took its ubiquitin-like domain 1 (Ubl1)[42], and produced a construct with it fused to a 6xHis tag and GFP.

For this experiment, we used condensates composed of N or pN and the 1-1000 RNA fragment. We added a small amount of GUVs and membrane protein fragments to the samples – either Nsp3 or M fragments or a control solution (Figure 2B). We observed the GFP signal from the membrane proteins become localized to the surface of GUVs, confirming tethering of the membrane protein fragments. Next, we used optical tweezers to control the position of condensates, moving them to and holding them at the GUV surface. We then attempted to pull the condensates off the surface and observed whether they remained bound or were mobile. For example, in a sample with pN, 1-1000 RNA, GUVs, and Nsp3 fragments, we brought condensates composed of pN and 1-1000 RNA to the GUV and observed as the condensates wet the surface (Figure 2C).

We defined five types of interactions between condensates and membranes (Figure 2D legend): 1) With no interaction, the optical tweezer can move condensates away from a surface it was in contact with. 2) With only binding, we observe the condensates remain attached to the membrane surface even when the optical tweezer is attempting to dissociate the two, but no additional condensate – membrane interactions occur. 3) During membrane wrapping, the condensate binds to the membrane and the membrane surrounds the condensate over time. 4) In partial wetting, the condensate not only binds to the membrane surface but also partially deforms, expanding the area of contact between the condensate and membrane. 5) Finally, in complete wetting, the condensates totally wet the membrane surface, forming a thin layer of protein and RNA condensate.

We found that if no fragments of membrane proteins (Nsp3 or M) are present, no interaction occurs between N and RNA condensates and the GUV surface, regardless of the phosphorylation status

of N (Figure 2D and Videos S1-2). This suggests that N or pN and RNA condensates have no intrinsic ability to interact with lipid membranes of the composition tested. In contrast, when the Nsp3 fragment is at the surface of GUVs, we observe condensates composed of both N and pN binding to the membrane surface (Videos S3-4). With unmodified N, condensates with 1-1000 RNA only partially wet the surface. Condensates with phosphorylated N completely wet the surface, forming a thin layer of condensed material. This behavior of pN and RNA condensates resembles the formation of a layer of protein on vROs that is observed in infected cells[20]. Importantly, our results hint that phosphorylation of N modulates the material properties of N condensates, shifting the behavior observed from partial to complete wetting. The thin layer of N that is observed surrounding vROs in infected cells may be condensed pN wetting the surface due to pN-Nsp3 interactions.

When we repeated the experiment with the M fragment, we observed an important difference in binding based on the status of N phosphorylation: while condensates with unmodified N bound to the M-coated GUV surface, condensates with pN did not interact with the surface (Videos S5-6). Therefore, phosphorylation of N may have unexpected effects beyond modulating condensate material properties: it can act as a switch to prevent binding of pN to membrane surfaces displaying the viral Membrane protein, where new virion formation typically occurs. (We investigate how phosphorylation affects protein-protein interactions between N and M or Nsp3 in Figure 3). When condensates with N and 1-1000 RNA interacted with M coated GUVs, we observed binding (6/10 events) or membrane wrapping (4/10 events) (Figure 2E), the difference between either case likely driven by the membrane tension of the GUVs. In the cases where membrane wrapping occurs, the protein and RNA condensates are partially engulfed into GUVs in the time scale of minutes. The events of membrane wrapping are especially intriguing, given that they resemble the direction of membrane bending required for encapsidation. These observations are consistent with prior EM studies showing that RNPs may contribute to membrane bending after recruitment to the membrane by M[47,48].

We quantified the affinity between condensates and GUVs by measuring the geometric factor that considers the contact angles along the contact line between the GUV surface, the condensate, and the external solution as well as the intrinsic contact angle between condensate and GUV (Figure 2F-H)[32]. These are determined by the material properties of the condensate, the strength of interaction between

condensate and membrane surface, and the membrane tension of the GUV. No interaction between condensates and the membrane results in the highest geometric factors. An intermediate geometric factor is found with N condensates and Nsp3 fragments, where partial wetting is observed, and N condensates with M fragments, where either binding or membrane wrapping are observed. A drastic reduction in geometric factor occurs with pN and Nsp3, where complete wetting occurs. The different degrees of interaction also impact the intrinsic contact angle between condensate and GUV. Partial wetting or membrane wrapping cause an intermediate reduction in the angle, while complete wetting causes a drastic reduction in the angle (Figure 2H). Overall, with this panel of condensate compositions and membrane surfaces, we were able to reproduce several behaviors that N displays during the viral lifecycle.

Phosphorylated N cannot bind to the SARS-CoV-2 Membrane protein

Given our observation that pN condensates did not bind to GUVs with M fragments, we examined whether phosphorylation affects protein-protein interactions between N and M or Nsp3. Several groups have sought to understand the binding mechanism between coronavirus N and M proteins[45,46], but no information is available on the effect of phosphorylation of N on its interaction with M. A stretch of amino acids (168–208) within the linker region of N was identified as critical for N-M interactions in the SARS-CoV-1 virus[45]. More recently, the linker domain of the SARS-CoV-2 N was shown to be necessary for N to co-phase separate with M[46]. Together, these studies point to a potential role of the SR-rich domain of N in interacting with M. Our results from Figure 2 suggest that phosphorylation of the SR region of N may inhibit binding between N and M.

We performed a partitioning experiment using confocal microscopy (Figure 3A). We added the fluorescently tagged M fragment or Nsp3 fragment to N or pN and observed the partitioning of the membrane protein fragments into condensates (Figure 3B-C). We confirmed that M has a much stronger affinity to unmodified N than to pN. Unmodified N binds to M independent of the presence of viral RNA fragments, though phase separation is promoted by the presence of 1-1000 RNA. We observed contrasting results with phosphorylated N mixed with M. First, M does not drive the condensation of pN without addition of RNA. Second, M does not partition preferentially into condensates composed of pN

and viral RNA (partition coefficient for M is 9.8 ± 0.3 in N + 1-1000 RNA condensates vs. 0.3 ± 0.1 in pN + 1-1000 RNA condensates; partition coefficient is defined as the ratio of average fluorescence intensity inside vs. outside the condensates). Given that M likely interacts with residues around N's SR domain[45], it is not surprising that phosphorylation of the SR region affects binding between the two proteins. These results are intriguing because they suggest a mechanism for timing of viral assembly. As noted above, a majority of N within infected cells is phosphorylated, but N included within new virions is unmodified[15]. pN may not be incorporated into newly formed virions because this protein is unable to bind M and anchor the RNP to the membrane at the site of viral assembly.

As a comparison, we also investigated whether phosphorylation affects the partitioning of Nsp3 protein's Ubl1 domain into N or pN condensates. Previous reports showed that Nsp3 Ubl1 domain partitions into condensates composed of both N and a phosphomimetic version of N[17]. Our results qualitatively agree with these findings, although we found pN has a lower affinity than N for Nsp3, based on our measured partition coefficients (12.6 ± 0.1 for Nsp3 in N + 1-1000 RNA condensates vs. 2.2 ± 0.1 in pN + 1-1000 RNA condensates). Given the hypothesized role of N in delivering the viral genome to Nsp3-coated replication organelles following viral entry into cells, and given that the films of N observed adhered to replication organelles[20] are likely composed of phosphorylated N, it is not surprising that both unmodified and phosphorylated N bind to Nsp3.

Phosphorylation of N modulates the material properties of N condensates

Based on our membrane binding experiments, we hypothesized that phosphorylation makes N condensates more fluid, explaining their propensity to relax at the surface of GUVs. To explore the material properties of condensates, we first used Fluorescence Recovery after Photobleaching (FRAP). We photobleached either fluorescently labeled protein or RNA within a region of the condensate and observed how the fluorescence recovered over time. The advantage of using FRAP here is that it allows us to independently assess the dynamics of protein and RNA in our multi-component condensates. N bound to 1-1000 RNA recovers more slowly than pN bound to the same RNA (recovery half-life τ = 2.6 ± 0.1 min for N and 1.7 ± 0.1 min for pN) (Figure 4A-B and Supplemental Figure 3). In addition, the total recovery of N is lower compared to pN (62% vs. 94%), suggesting a pool of N is fixed to the RNA. Both

metrics suggest that pN has a greater mobility than N when bound to 1-1000 RNA. In contrast to the results obtained by photobleaching protein within condensates, we observed almost no recovery of the fluorescence when RNA was bleached (Figure 4A and C), independent of protein phosphorylation status. RNA appears to form a network onto which protein can bind and dissociate[49]. Individual RNA molecules may move locally but do not appear to diffuse long distances, likely due to their ability to form intermolecular base pairs. Overall, our FRAP results provide insight towards understanding the membrane interactions observed in previous experiments. Condensates composed of pN that wet surfaces also showed a greater protein recovery in FRAP experiments, suggesting that the dynamic movement of protein allows the condensates to reorganize at the surface of membranes over time.

To quantitatively assess how phosphorylation affects N condensate material properties, we turned to passive microrheology and micropipette aspiration. In passive microrheology, we embed 500 nm fluorescent tracer beads into condensates and track their movement. The mean squared displacement (MSD) of beads depends on their viscous and elastic environment[50]. Beads embedded within condensates composed of pN + 1-1000 RNA displayed a greater MSD at all lag times when compared to beads embedded in N + 1-1000 RNA condensates (Figure 4D and Supplemental Figure 4). The MSD of beads did not increase linearly with lag time for all samples, revealing that some condensates behave as viscoelastic fluids under the experimental conditions. Using the Generalized Stokes-Einstein Relation, we estimated viscous and elastic moduli. For N + 1-1000 RNA condensates, the elastic modulus dominates the viscous modulus at high frequencies (> 56 Hz). In contrast, for pN + 1-1000 RNA, the viscous modulus is dominant for all frequencies measured (Figure 4E – F). We then quantified the zero-shear viscosity of the samples, i.e., the limiting value for viscosity at 0 Hz. For condensates composed of N + 1-1000 RNA, we found a viscosity of 192 ± 3.6 Pa*s, while for condensates with pN, we measured a viscosity of 59 ± 3.4 Pa*s, representing a ~3x reduction in viscosity (Figure 4G and Supplemental Figure 5).

The change in viscosity upon phosphorylation of N may be due to modulation of protein-protein and/or protein-RNA interactions, the latter via either specific or nonspecific binding to RNA. We assessed each of these possibilities by testing the material properties of N or pN condensates with unstructured RNA (polyrA) or with 5% PEG8000, which acts as a crowding agent to drive N phase separation without

RNA (Supplemental Figure 2). Phosphorylation of N decreased the viscosity of condensates with polyrA from 64 ± 4.2 Pa*s to 12 ± 0.4 Pa*s, suggesting that nonspecific interactions between protein and RNA were disrupted. Furthermore, phosphorylation decreased viscosity of condensates with PEG8000 from 11 ± 0.7 Pa*s to 4 ± 0.3 Pa*s, suggesting that protein-protein interactions are also disrupted to some degree. We also quantified the terminal relaxation time of the condensate network, which is the inverse of the crossover frequency between the predominantly elastic and predominantly viscous regimes. At timescales below the relaxation time, the condensates behave as elastic materials. Elasticity is reduced by phosphorylation in both polyrA and 1-1000 RNA samples (Figure 4H). Condensates with N and polyrA or 1-1000 RNA have a relaxation time of 0.01 - 0.02 seconds, while condensates with pN have no measurable relaxation timescale, suggesting that phosphorylation disrupts the ability of N and RNA to crosslink (Supplemental Figure 6). The elasticity displayed by complexes formed between unmodified N and RNA may have a biological function in protecting the RNA from mechanical stress[51].

We confirmed our material property measurements using micropipette aspiration (MPA)[52,53]. We recorded how the length of the aspirated condensate in a micropipette changes as a function of time in response to an applied pressure. We quantified the viscosity for the different protein combinations and obtained the same trend and rank order that was observed using microrheology (Figure 4I and Supplemental Figure 7). (Viscosities quantified via MPA were consistently lower than the zero-shear viscosities obtained from microrheology; when the two data sets are plotted against each other, they have a linear fit with slope of 0.72 and R^2 of 0.99). Notably, MPA measurements also showed that pN condensates have lower viscosity than the corresponding N condensates. Together, our microrheology and micropipette aspiration results point to N and RNA condensates being viscoelastic fluids whose properties depend on both RNA type and phosphorylation status. Phosphorylation of N appears to loosen the network of interactions between N and RNA, thus reducing the viscosity and elasticity of condensates.

RNA type also modulates condensate material properties

We repeated experiments with a second viral RNA fragment to assess whether our results depend on RNA sequence and structure. We used N RNA, introduced previously, which encodes the N protein and is 1340 base pairs long. N RNA is an important viral RNA to test because it is abundant in

infected cells, and from a biophysical perspective, it is (1) longer than 1-1000 RNA, and as such has a higher ensemble diversity (which describes the diversity of conformations the RNA is predicted to fold into; it is predicted to be 198.5 for N RNA vs. 148.1 for 1-1000 RNA, based on ViennaRNA[54]), and (2) contains a different pattern of preferred binding sites for N[55]. These factors suggest that N RNA forms a more entangled network in condensates compared to 1-1000 RNA, resulting in the different condensate morphologies observed (Figure 1F). We found similar behavior between condensates with 1-1000 or N RNA (Supplemental Figure 8), both in terms of binding to GUVs with different membrane protein fragments, as well as their material response to phosphorylation (phosphorylation reduces viscosity and elasticity). These results suggest that the change in N condensate material properties and membrane interaction upon phosphorylation are not RNA structure dependent. Across experiments, we did observe that condensates with the longer N RNA were less likely to deform than their counterparts with 1-1000 RNA. This data hints that complexes of unmodified N and longer fragments of RNA, such as genomic RNA, would appear solid-like and with an important elastic response, which may play a role in mechanically protecting RNA within virions[51]. To further study these questions, additional analyses with varying RNA lengths and structures would be required.

Phosphorylation weakens binding between N and RNA by promoting linker-linker interactions

We have shown that phosphorylation of N results in condensates that more readily deform at membrane surfaces and that have a lower viscosity and elasticity, both likely driven by a loosening of the interaction network between protein and RNA. This change in interaction does not appear to be dependent on specific RNA structures, as phosphorylation also drastically softens condensates with unstructured polyrA (Figure 4G-I). We therefore asked how phosphorylation affects N, such that interaction between protein and RNA is diminished.

We leveraged fluorescence polarization to measure the binding affinity between N protein and fluorescently labelled RNA (Figure 5A-B). First, we assessed whether phosphorylation affects binding of N to a stem-loop structure (SL4) present in the 1-1000 RNA fragment. SL4 was identified as a preferred binding site for N's RNA binding domain[23,24]. Phosphorylation of N reduces the binding affinity to SL4 RNA, increasing the dissociation constant (K_D) from 10.9 ± 1.4 nM to 59.0 ± 0.9 nM. Although this is a six-

fold reduction in binding affinity, the concentrations at which our membrane interaction and material property experiments were conducted are well above the nanomolar K_Ds measured, and therefore this change in binding cannot explain the changes observed. Next, to test the hypothesis that nonspecific binding between protein and RNA is disrupted by phosphorylation, we measured the binding affinity between N or pN and a 30-base polyrA. Phosphorylation causes a twenty-fold change in K_D from 71.7 ± 0.8 nM to 1571.0 ± 2.1 nM, larger than that observed for the SL4 RNA. We conclude that phosphorylation reduces N's interaction with unstructured RNA more so than structured RNA. Importantly, for both polyrA and SL4, phosphorylation of N also reduced the maximum polarization. This suggests a greater rotational freedom in the protein-RNA complexes formed with pN that could be driven either by the formation of a more compact complex or a conformation in which the protein-bound RNA retains more rotational mobility[56]. We anticipated that phosphorylation would weaken binding between N and RNA due to electrostatic repulsion. However, our fluorescence polarization results suggest that phosphorylation may also be inducing a conformational change in N which affects its RNA binding properties.

We therefore used single-molecule Förster Resonance Energy Transfer (smFRET) to explore the conformation of N[8]. First, for full-length N, we confirmed that phosphorylation does not affect the conformation of the dimerization domain[57] or the tendency of N to dimerize (Supplemental Figure 9). Next, we used smFRET to study the conformation of the linker region. We probed two constructs of N with fluorescent labels flanking the linker region (at residues 172 and 245): full-length N and truncated N^{1-246}, which lacks the dimerization and C-terminal disordered domains. We performed experiments at two protein concentrations: low concentration, at which N is in its monomeric form, and high concentration, at which dimers form if the dimerization domain is present. We measured the distribution of transfer efficiencies for each protein construct at each concentration (Figure 5C-D). The distributions represent a dynamic ensemble of conformations, as supported by the corresponding analysis of donor lifetime vs. transfer efficiency (Supplemental Figure 10). Therefore, we used the mean transfer efficiencies to calculate the root mean square distance (RMSD) between labelled residues, which can be compared across samples to understand the degree of expansion of the linker (Figure 5E). Consistent with previous measurements of the same constructs[8], we observed a mean transfer efficiency of approximately 0.6 for full-length N and 0.75 for N^{1-246}. These values represent rather compact ensembles, despite the

significant net charge content of the interdye sequence, and points to interactions between the linker and the N2 domain[8]. For both concentrations tested, presence of the dimerization domain (N4) causes expansion of the linker, suggesting the nearby folded domain represents an excluded volume that restricts the linker's conformation. We also found that phosphorylation causes an additional expansion of the linker region, which is unexpected given the introduction of negative charges to a cationic sequence, though this may result from the number of bulky phosphate groups or a weaker interaction with N2[58]. Importantly, the degree of expansion due to phosphorylation is greatly reduced in the full-length construct under dimer conditions. Formation of the dimer may destabilize interactions with N2 to such a degree that phosphorylation can add little to such destabilization compared to other cases where the N2 interaction was stronger. Another possibility is that intermolecular interactions between monomers within a pN dimer may drive bending of the linker that counteracts the expansion caused by phosphorylation. To evaluate these hypotheses, we investigated the conformation of the N dimer entirely.

Due to the largely disordered nature of the N protein dimer, we used Small Angle X-ray Scattering (SAXS) to study how phosphorylation affects the dimer structure. First, we found a significant decrease in radius of gyration of N vs. pN dimers, from 58.0 ± 1.0 Å for N to 53.3 ± 2.5 Å for pN, a finding supported by both the pair distance distribution and the Guinier approximation (Figure 5F-G and Supplemental Figure 11-12). Next, analyzing normalized Kratky plots confirms both N and pN display behavior typical of a multidomain protein with flexible linkers (Figure 5H). The elevated tail for N indicates greater extension of the protein compared to pN. Using the scattering data to construct bead models for N and pN allows us to visualize these changes (Figure 5I-J and Supplemental Figure 13). Our bead models show a new region of electron density between monomers within pN dimers, suggesting that a new interaction between the linkers takes place in pN dimers that is not present in N dimers. Binding between arginine residues and phosphate groups across members of a pN dimer may be the basis for the new intermolecular interactions observed. This agrees with previous molecular simulations data that found a phosphorylation-induced increase in intra- and inter-molecular contacts in pN due to the formation of salt bridges between phosphate groups and arginine side chains[22]. We speculate that this new interaction between monomers may be interfering with N's ability to bind to RNA. The more compact conformation of pN dimers and reduced affinity between protein and RNA[9] may explain our earlier observations from the

binding affinity assay and material property measurements. Therefore, this new model ties together the conformational change of N upon phosphorylation with its reduced ability to interact with RNA, which in turn affects its condensate material properties and its form when interacting with membranes.

Discussion

Despite significant interest, there is still limited knowledge about how phosphorylation regulates the conformation, dynamics and function of SARS-CoV-2 N protein, especially in relation to membrane interaction. This is an important question because N has been observed in two membrane-associated forms inside cells: 1) adhered to viral replication organelles in a dynamic thin film and 2) bound to viral genomic RNA in solid-like complexes that associate with the ERGIC membrane during viral budding [20,21]. To gain insight into these two states of the N protein, we focused on the SR region, which is known to be heavily phosphorylated in infected cells but unmodified during viral assembly[15]. Phosphorylation has been shown to influence the compactness of RNP complexes and the strength of RNA binding[29].

In this work, we argue that the phosphorylation state of N determines its two membrane-associated behaviors in infected cells, namely being adhered to membrane surfaces and being tightly bound to RNA when engulfed into new virions. Our experiments show that phosphorylation affects the behavior of N in two ways: first, it weakens the ability of N to interact with the viral M protein, and second, it results in deformable protein and RNA condensates that wet a membrane surface. We investigated the material properties of N vs. pN and RNA condensates and showed that condensates with phosphorylated N are less viscous and elastic than their unmodified counterparts. This trend in material properties of N and RNA condensates was independent of whether structured or unstructured RNA was present. We then showed that this change in material properties was due to weakening of N's binding to RNA following phosphorylation. We studied N at a molecular level and identified that phosphorylation results in new interactions between the SR linkers of the two monomers in a dimer, thus interfering with the protein's ability to interact with RNA. Our findings tie together an understanding of how phosphorylation acts as a switch controlling the conformation and behavior of N during viral replication (Figure 6).

Our results are distinct from recently published data on the effect of phosphorylation on the molecular conformation of N determined using NMR. Botova et al. found a rigidification of the SR region

upon phosphorylation that their data suggests is a result of new interactions with the RNA binding domain[58]. Their conclusions are due to the similarity in the chemical shift perturbations observed when N is phosphorylated vs. when RNA binding occurs. However, the rigidification of the SR region could also be due to the presence of bulky phosphate groups. Though new interactions between N's RNA binding domain and the linker region could be overlooked by our SAXS-derived reconstruction given its low resolution, our results point to a larger conformational shift of the dimer. Stuwe et al. also studied the effect of phosphorylation on N using NMR, though the construct studied lacked the N-terminal RNA binding domain, thus potentially skewing the analysis of intra- and inter- molecular interactions[59]. They found that phosphorylation changes the behavior of a leucine-rich helix (LRH) found in N's linker: in unmodified N, higher order oligomers form through LRH self-interaction that is significantly weakened by phosphorylation. In contrast with these results, our data presents an alternative model in which phosphorylation of N promotes intermolecular interactions between the SR regions of monomers within a dimer and thus disrupts non-specific interaction between pN and unstructured RNA. We do not observe a significant change in the oligomerization behavior of N following phosphorylation (Supplemental Figure 9).

A recent study suggested that the N in cells is sequentially phosphorylated by host kinases SRPK1, GSK-3, and CK1[16]. Inhibiting SRPK1 was found to reduce viral replication, while blocking GSK-3 activity decreased replication in cells and reduced infection in patients[16,60]. However, given the wide range of functions of these human kinases, inhibiting phosphorylation may not be a viable path to treatment of SARS-CoV-2 infection. Our results suggest an alternative approach to inhibiting viral replication. Given the important role of RNA structure in modulating the material properties of N and RNA condensates, molecules that disrupt viral RNA structure may be potential treatments for viral infection. For example, Vögele et al. identified a molecule that disrupts the double stranded structure of stem loop 4 (SL4) in viral RNA[61]. Further investigation is needed to assess whether this type of disruption modulates the material properties of N and RNA condensates to an extent that impairs N's functions in viral replication.

Although significant progress has been made in understanding the molecular determinants of a condensate's material properties, condensates studied *in vitro* are often much simpler (e.g., using simple RNA models such as polyrA) than those found in cells, which are often a complex mixture of proteins and structured RNA or DNA[62,63]. Therefore, we have limited understanding of how material properties and

function are determined for condensates composed of protein and RNA. Here, using a more physiological reconstitution strategy, we explored how a naturally occurring system of protein and RNA interact to determine the resulting condensate's viscosity and elasticity. These findings can be applied to better understand not only SARS-CoV-2-related condensates, but also other protein-RNA condensates.

In conclusion, we have investigated the connection between a protein's molecular conformation, its material properties when phase separated with RNA, and its membrane-associated behavior. We show that phosphorylation may act as a switch to toggle N between its two membrane-associated states during viral replication. This can be traced back to a change in the protein's conformation that then impacts its interaction with RNA and its material properties as a condensate. Given the complexity of the system studied, further investigations are still needed to better understand how our results can be expanded to other N protein-RNA interactions that occur in infected cells, considering factors such as the presence of human mRNA, other viral subgenomic RNAs that do not promote phase separation, and the much longer viral genomic RNA.

Acknowledgements

We thank Christine Roden and Amy Gladfelter for helpful discussion, for sharing plasmids for making RNA fragments and fluorescently labeled viral RNA; Mihai Solotchi and Smita Patel for assistance with fluorescence polarization experiments and helpful discussions; Gabriela Tirado-Mansilla for assistance preparing SAXS samples; Bineet Sharma for help with GUV production; Srinivas Chakravartula and Haiyan Zheng for assistance with mass spectrometry; Kevin Corbett and Qiaozhen Ye for sharing the GFP-Mfragment plasmid; and Jean Baum and Vikas Nanda for helpful discussion. This work was supported by NIH grants R35GM142903 (to B.S.), R35GM147027 (to Z.S), R35GM138296 (to A.G.) and National Science Foundation grant DMREF-2118860 (to S.M. and A.G.). X-ray scattering measurements were done at the NSLS-II beamline 16-ID (LiX) at Brookhaven National Laboratory. The LiX beamline is supported by an NIGMS P30 Grant (P30GM133893), NIH Grant S10 OD012331, the DOE Office of Biological and Environmental Research (KP1605010), and the DOE Office of Science, Office of Basic Energy Sciences Program under contract number DE-SC0012704 to CBMS. Figure 1A: Created in BioRender. Favetta, B. (2024) BioRender.com/o21g999. Figure 2A-B: Created in BioRender.com. Figure 3A: Created in BioRender.com. Figure 6: Created in BioRender. Favetta, B. (2022) BioRender.com/382j936.

Author Contributions

BF: conceptualization, experimental design, data collection and analysis, writing—original draft, writing—review and editing; HW: data collection for MPA experiments; JC and AS: experimental design, data collection and analysis for smFRET experiments; MB: data analysis for microrheology experiments; CR: data collection and analysis for SAXS experiments; SM: experimental design, data collection, analysis and supervision for SAXS experiments; AJG: supervision of SAXS data analysis and funding acquisition; ZS: supervision, experimental design for MPA and GUV experiments and funding acquisition; BSS: conceptualization, supervision, experimental design, data analysis, writing—original draft, writing—review

and editing, funding acquisition.

Declaration of Interests

The authors declare no competing interests.

Figure Captions

Figure 1: Phosphorylation of the SARS-CoV-2 Nucleocapsid protein (N). A) Schematic of full-length SARS-CoV-2 Nucleocapsid protein (N) used in experiments, showing N1, a disordered domain; N2, RNA binding domain; N3, disordered linker domain containing the Serine-Arginine-rich (SR) region; N4, dimerization domain; and N5, a disordered domain. B) Sites of phosphorylation in the SR region of the N3 domain. Our experiments used two kinases – SRPK1 and GSK3β – resulting in a maximum of 10 phosphorylation sites. C) Hypothesized form and roles of N and phosphorylated N (pN). pN may have dynamic functions, forms liquid-like droplets with RNA and may localize to the surface of replication organelles. Unmodified N forms solid-like, spherical assemblies with genomic RNA and facilitates new virus encapsulation. N's form with RNA was characterized by Carlson et al., 2020 using light and electron microscopy. D) A diagram of the SARS-CoV-2 lifecycle. Following viral entry (1), the genome is uncoated (2) such that it can be read. Viral RNA is stored within viral replication organelles (3) wherein RNA transcription and replication may be occurring. N binds to and condenses genomic RNA exiting these organelles (4). In parallel, viral structural proteins are produced (5), in preparation for viral encapsulation (6) and exit (7). E) Main RNA fragments used in experiments are the first 1000 bases from the 5' end of the viral genome and the 1340 base fragment encoding N. F) Droplets with varied morphologies form upon mixing 40 µM N (5% Alexa Fluor 647 labeled) and 300 nM RNA fragments (5% Cy3 or Cy5 labeled) at 37˚C. Scale bar = 5 µm.

Figure 2: N condensate interaction with membranes. A) Fragments of the membrane proteins used to test membrane interactions: C-terminal endodomain of the Membrane (M) protein and the ubiquitin-like domain (Ubl1) of the Nsp3 protein. Both protein fragments are fused to 6x Histidine tag and GFP. B) Schematic of the experimental setup showing the M or Nsp3 protein fragment tethered to the giant unilamellar vesicle (GUV) surface. Condensates composed of 40 µM N or pN plus 300 nM RNA are moved to the GUV surface using optical tweezers. C) Representative widefield images showing that Nsp3 fragments preferentially localize to the GUV surface (left) and condensates composed of pN and 1-1000 RNA wet the surface of GUVs after being delivered to the surface using optical tweezers (OT) (right). White dashed line added to denote the GUV surface. D) Representative widefield images showing the interaction between condensates and membranes over time, for N vs. pN, and comparing GUVs with no membrane protein, M fragment, and Nsp3 fragment. GUVs are labeled in green, and condensates (Cond.), in blue. Interaction type is qualitatively classified. E) Timelapse imaging showing several condensates (blue stars) being dragged by optical tweezers to the surface of a GUV, to which they bind. Optical tweezers can be used to pull bound condensates which results in deformation of the GUV surface (arrow). Membrane wrapping occurs in one case. F) Sketch showing the parameters that define the geometric factor (Φ) and intrinsic contact angle (θin). Interaction leads to the formation of a contact line between the condensate interface and membrane. Contact angles $\theta c + \theta e + \theta i = 360°$ and we can calculate Φ to describe the degree of wetting. Wetting can also be characterized by θin between condensate and membrane surfaces. G) Quantification of the geometric factor from each combination of condensate composition and membrane surface. Interactions that lead to membrane wrapping, partial wetting, or complete wetting result in reduced geometric factors. H) Intrinsic contact angle from each combination of condensate composition and membrane surface. n = 10 condensate-membrane interactions from n = 3 independent trials. Individual data points are shown for each interaction event. The lines indicate the median, lower quartile, and upper quartile. Scale bars = 5 µm.

Figure 3: N and pN interaction with membrane proteins, M and NSP3. A) Schematic of the experimental setup where 6xHis-GFP-$M^{104-222}$ or 6xHis-GFP-$NSP3^{1-111}$ is added to a condensate sample and partitioning of GFP-tagged protein is quantified using confocal microscopy. B) Representative

confocal images from condensates composed of 40 µM N or pN plus either no RNA or 300 nM RNA; plus either 2 µM 6xHis-GFP-$M^{104-222}$ or 6xHis-GFP-$NSP3^{1-111}$. 6xHis-GFP-$M^{104-222}$ binds to N but not pN condensates while 6xHis-GFP-$NSP3^{1-111}$ partitions in regardless of choice of N vs. pN. Normalized line profiles across condensates, representing averages of at least n = 20 condensates from 3 independent trials. Scale bars = 5 µm. C) Quantification of partitioning of GFP-tagged proteins into N or pN condensates by dividing average fluorescence inside condensates (if any) by the average background fluorescence. Error bars represent one standard deviation (±1 s.d.). p values were determined using two-way ANOVA followed by post hoc Tukey's test. *$p < 0.01$.

Figure 4: Phosphorylation modulates material properties of N and RNA condensates. A) Fluorescence recovery after photobleaching (FRAP) of N and RNA condensates, in which 5% of N/pN is labeled with Alexa-647 and 5% of RNA is labeled with Cy-3. pN recovers to a greater extent over time when compared to N, while in neither case does RNA signal recover. Scale bar = 5 µm. B) Quantification of FRAP of protein in N vs. pN condensates (n = 3 independent trials). C) Quantification of FRAP of RNA in N vs. pN condensates (n = 3 independent trials). D) Ensemble MSD versus lag time (prior to noise correction) for the protein and RNA combinations tested in this study. Inset: Representative trajectories from two-dimensional particle tracking showing Brownian motion of beads in N vs. pN condensates with 1-1000 RNA. Each tick represents 5 nm. E) Plot with the average viscous modulus (G'', red) and the average elastic modulus (G', blue) of N + 1-1000 RNA condensates as calculated from the MSDs (n ≥ 10 videos from 3 independent samples) after noise correction. F) The average viscous and elastic moduli after noise correction for pN + 1-1000 RNA condensates showing no crossover frequency in the range studied. G) The zero-shear viscosity of the protein and RNA condensates studied, calculated from the particle-tracking results after noise correction. Data from n ≥ 10 videos from 3 independent trials. H) Quantification of the timescales at which the elastic modulus dominates (color) versus the viscous modulus dominates (grey) in protein and RNA condensates. I) Viscosity of the protein and RNA condensates from micropipette aspiration. n = 3 independent trials. Error bars represent one standard deviation (±1 s.d.).

Figure 5: N protein phosphorylation weakens RNA binding affinity due to change in protein conformation. A) Quantification of binding affinity between N vs. pN and the viral stem loop 4 RNA (SL4) based on a change in normalized fluorescence polarization (minimum polarization set to 0). n = 3 independent trials. B) Quantification of binding affinity between N vs. pN and unstructured 30 base polyrA from normalized fluorescence polarization. n = 3 independent trials. C) Representative distributions of transfer efficiency for full-length N (top) and pN (bottom) at low concentration (100 pM labeled protein) and high concentration (100 pM labeled protein + 1 µM unlabeled protein) with fluorescent dyes flanking the linker region at residues 172 and 245. D) Representative distributions of transfer efficiency for N^{1-246} (top) and pN^{1-246} (bottom) at low concentration (100 pM labeled protein) and high concentration (100 pM labeled protein + 4 µM unlabeled protein) with fluorescent dyes flanking the linker region at residues 172 and 245. E) Root mean squared inter-dye distance obtained from the mean transfer efficiencies for unmodified and phosphorylated full-length N and N^{1-246}. F) Representative pairwise interatomic distance distribution P(r) derived from SAXS for N and pN. N or pN concentration = 3 mg /mL. G) The maximum distance (Dmax) and radius of gyration (Rg) for N and pN derived from the pair distance distributions. p values were determined using two-sided student's t-test; asterisk indicates $p < 0.05$. H) Normalized Kratky plot comparing the scattering of N vs. pN, indicating a structural change has occurred due to phosphorylation. Concentrations shown for N or pN are 1, 1.5, 3, and 4 mg/mL from lighter to darker. I) Bead model representation for the N dimer developed from SAXS results (left) and hypothesized conformation of N (right). J) Bead model representation for the pN dimer developed from SAXS results (left) and hypothesized conformation of pN highlighting new intermolecular interactions (right). Error bars represent one standard deviation (±1 s.d.).

Figure 6: Model of N protein form and membrane-associated state during the viral lifecycle. Inside the cell (1), the vast majority of N is found in its phosphorylated form, localized to the surface of viral replication organelles (2). Phosphorylation promotes linker-linker interactions across N dimers that weaken interaction between N and RNA (inset, left). This looser protein-RNA interaction network within condensates results in a relatively low viscosity and elasticity that may facilitate the molecular diffusion needed during RNA transcription and replication. A second population of N that is destined to form new

virions binds to new viral genomic RNA (gRNA) and condenses RNA into small spherical complexes (3). This unmodified protein binds tightly to gRNA through both specific and nonspecific interactions (inset, right). These assemblies have high viscosity and elasticity that may support a protective function of N towards gRNA. The gRNA and N capsid is engulfed by the ERGIC membrane, facilitated by N and M interactions (4). New virions exit the infected cells (5).

Resource Availability

Lead contact: Requests for further information and resources should be directed to and will be fulfilled by the lead contact, Benjamin S Schuster (benjamin.schuster@rutgers.edu).
Materials availability: Plasmids generated in this study will be deposited to Addgene (links will be made available upon publication).
Data and code availability: All the quantitative analyses discussed in this paper were generated based on data and computer codes that will be made publicly available (links will be made available upon publication).

Supplemental information

Document S1. Table S1, Figures S1–S13 and Supporting Methods

Supplemental videos 1-6, related to Figure 2.

Methods

Cloning

All genes of interest were cloned into pET vectors in frame with N-terminal 6x-His tags. A TEV protease site was inserted between the 6x-His tag and the Nucleocapsid protein coding sequence. Constructs were cloned by DNA assembly (NEBuilder HiFi DNA Assembly Master Mix; New England Biolabs). Gene sequences were verified by Sanger sequencing (Genewiz).

Protein expression and purification

For bacterial expression, plasmids were transformed into BL21(DE3) competent E. coli (New England BioLabs). Colonies picked from fresh plates were grown for 12 hours at 37 °C in 5 mL LB while shaking at 250 rpm. This starter culture was then used to inoculate 0.5 L cultures. Cultures were grown overnight in 2 L baffled flasks in Terrific Broth medium (Fisher Scientific) supplemented with 4 g/L glycerol at 18°C while shaking at 250 rpm. Once the OD_{600} reached approximately 1, expression was induced with 500 μM isopropyl β-D-1-thiogalactopyranoside (IPTG). The pET vectors used contained a kanamycin

resistance gene; kanamycin was used at concentrations of 50 µg/mL in cultures[64]. After overnight expression at 18 ˚C, bacterial cells were pelleted by centrifugation at 4100 x g at 10 ˚C. Pellets were resuspended in lysis buffer (1 M NaCl, 20 mM Tris, 20 mM imidazole, EDTA-free protease inhibitor, pH 7.5) and lysed by sonication while on ice. Lysate was clarified by centrifugation at 25000 x g for 30 minutes at 10 ˚C. The clarified lysate was then filtered with a 0.22 µm filter.

Proteins were purified using an AKTA Pure FPLC with 1 mL nickel-charged HisTrap columns (Cytiva) for affinity chromatography of the His-tagged proteins. For N protein, after injecting proteins onto the column, the column was washed with 15 column volumes of 3 M NaCl, 20 mM Tris, 20 mM imidazole, pH 7.5. For all other proteins, after injecting proteins onto the column, the column was washed with 5 column volumes of 500 mM NaCl, 20 mM Tris, 20 mM imidazole, pH 7.5. Proteins were eluted with a linear gradient up to 500 mM NaCl, 20 mM Tris, 500 mM imidazole, pH 7.5. Histidine tags were cleaved from the N protein using TEV protease during dialysis. TEV protease was added to proteins and dialyzed overnight using 10 kDa MWCO membranes (Slide-A-Lyzer G2, Thermo Fisher) into 300 mM NaCl, 20 mM Tris, 20 mM imidazole, 5mM DTT, pH 7.5 buffer at 4°C. The reaction mixture was purified using a nickel resin gravity column (HisPur Ni-NTA Resin, Thermo Fisher) and the flow through was collected. Flow through aliquots were concentrated and buffer exchanged into storage buffer (300mM NaCl, 20 mM Tris-HCl, pH 7.5) using a 10kDa MWCO centrifugal filter (Amicon Ultra, Sigma). Proteins were either reserved for the phosphorylation protocol or snap frozen in liquid N_2 in single-use aliquots and stored at -80 °C.

SDS-PAGE

For chromatographically purified proteins, SDS-PAGE was run using NuPAGE 4-12% Bis-Tris gels (Invitrogen) and stained using a Coomassie stain (GelCode Blue Safe Protein, Thermo Scientific).

Fluorescent labeling of N protein

Purified N protein was dialyzed into PBS buffer with 0.1 mL sodium bicarbonate per 1 mL protein solution. Protein was then labeled by adding a 3:1 molar ratio of Alexa 647 NHS ester (stored in DMSO). The mixture was incubated at 4°C for 1 h with rocking. Unbound dye was removed by size exclusion chromatography (Superdex 200 Increase 10/300 GL, Cytiva). For phase separation assays, percent of dyed protein was adjusted to 5% of total by dilution with undyed protein.

Phosphorylation protocol

~80 μM N protein was prepared in a buffer containing 300 mM NaCl, 20 mM Tris, 1mM dithiothreitol (DTT), 10 mM $MgCl_2$, and 2 mM ATP in a 200 μL reaction mixture. 5 μL GSK-3β and 5 μL SRPK were added to the mixture. After incubation at 37°C for 120 min, phosphorylation was confirmed using a SuperSep Phos-tag acrylamide gel (FujiFilm Wako Chemicals). Enzymes were removed from the reaction mixture using GST-based affinity chromatography. Briefly, 1 mL of gluthathione resin (Glutathione Sepharose 4B, Cytiva) was packed in a gravity column. The column was washed with 300mM NaCl, 20mM Tris, pH 7.5 buffer. The 200 uL of reaction mixture was diluted to a total of 2 mL using wash buffer and poured into the column. The column flow through was collected. The column was washed with an additional 1 mL of wash buffer, which were collected. The flow through and wash fractions were combined and the 3 mL of solution containing phosphorylated N protein was concentrated and buffer exchanged using an Amicon Ultra 0.5 mL 10K MWCO centrifugal filter, according to manufacturer instructions.

RNA In vitro transcription protocol

RNA production was carried out according to established protocols[65]. Templates were gifted from the Gladfelter lab where they were synthesized (IDT) and cloned into pJet (ThermoFisher Scientific K1231) plasmids using blunt end cloning. Directionality and sequence were confirmed using Sanger sequencing (Azenta). Plasmids were linearized and then amplified using PCR. 10 ng of plasmid was used as starting material and primers are noted in the Supplemental Materials. Melting temperatures for the 1-1000 and N fragments were 69˚C. 5 µl of PCR product was loaded onto an agarose gel to determine size and purity using SYBR™ Gold Nucleic Acid Gel Stain and NEB 1 kb Plus DNA Ladder. If the PCR product was pure then the sample was purified (NEB DNA Clean-up kit). 100 ng of purified DNA was used as a template for *in vitro* transcription (NEB E2040S) carried out according to the manufacturer's instructions. Following incubation at 37°C for 18 h, *in vitro* transcription reactions were treated with DNAse (NEB M0303L) according to the manufacturer's instructions. Following DNAse treatment, reactions were purified with an RNA purification kit (NEB T2040L). Purified RNA was verified for purity and size using an agarose gel and RNA Gel Loading Dye (NEB B0363S) and RiboRuler High Range RNA Ladder (Thermo Scientific SM183). Concentration was measured using a Nanodrop One spectrophotometer (ThermoFisher Scientific).

Fluorescently labeled RNA was gifted by the Gladfelter lab. Cy3 RNA was transcribed from the same template used above and using the same protocol described above, but with the addition of 0.1 µL of Cy3 labeled UTP to each reaction (Sigma PA53026).

Microscopy

For microscopy experiments, protein samples were prepared as follows: N or pN protein aliquots were thawed at room temperature. Proteins were then mixed with a combination of 20 mM Tris, 150 mM NaCl, pH 7.5 and 20 mM Tris, 0 mM NaCl, pH 7.5 buffers and the desired RNA (if any), stored in water, to obtain a final solution containing 150 mM NaCl and the protein and RNA concentrations desired for the experiment (40 µM protein and 300 nM viral RNA or 1 mg/mL polyrA unless otherwise noted). All experiments were conducted with a buffer concentration of 20 mM Tris, 150 mM NaCl, pH 7.5. Protein concentrations were measured based on their absorbance at 280 nm using a Nanodrop spectrophotometer (ThermoFisher).

Protein samples were plated on 1.5 thickness slides that were coated with 5% Pluronic F-127 (Sigma-Aldrich) for a minimum of 10 minutes. The slides were washed with buffer solution prior to plating the protein samples. A silicone spacer (0.5 mm) and a microfluidic temperature controller (Cherry Biotech) were attached to the slide and the temperature of the sample was set to 37˚C during observation.

Confocal imaging was performed on a Zeiss Axio Observer 7 inverted microscope equipped with an LSM900 laser scanning confocal module and employing a 63x/1.4 NA plan-apochromatic, oil-immersion objective. GFP was excited to fluoresce with a 488 nm laser, Cy3 and Alexa-567 with a 561 nm laser and Cy5 with a 630 nm laser. Confocal fluorescence images were captured using GaAsP detectors. Transmitted light images were collected with either the ESID module or an Axiocam 702 sCMOS camera (Zeiss), in both cases using a 0.55 NA condenser.

Droplet image analysis

Image analysis and data processing for Figures 2, 3 and 4 A-C and Supplemental Figures 2 and 8 B-C were performed in MATLAB R2023a. The fluorescence intensity profile of the condensates with fluorescently labeled proteins was measured by using the Hough Transform to identify droplet locations and drawing a line that spanned the droplet diameter plus 1/4th of a radius length in each direction across

the droplets. Line-scan graphs were generated in MATLAB. Total intensity and partitioning graphs were generated in MATLAB. Condensate perimeter and area were calculated using MATLAB's inbuilt regionprops function.

Giant unillamellar vesicle electroformation

Giant unilamellar vesicles were prepared by electroformation[66]. Briefly, 20 uL of a lipid solution containing 60% DOPC, 25% DOPE, 10% DOPS, 5% Ni-NTA in chloroform was prepared. ~10 µL lipid solution was spread onto indium tin oxide (ITO)-coated glasses and dried under vacuum for 12 h. The plates were assembled into a chamber with a Teflon spacer and the swelling solution (~1 mL of 300mM sucrose) was introduced. For electroformation, a sinusoidal electric field of 2.0 Vpp and 10 Hz was applied using a function generator for 2.5 h, after which the frequency was reduced to 5 Hz for 30 min. In all cases, osmolarities of sucrose solutions matched the osmolarities of the condensate NaCl solutions.

Contact angles measurement and geometric factor calculation

A detailed explanation of the contact angles used in this work has been published elsewhere[32]. Briefly, we measured the three contact angles θ_c, θ_e, θ_i from fluorescent images of GUVs and condensates (for samples with GFP) or from brightfield images (for samples without GFP). From these angles, we calculated the geometric factor, Φ. From Mangiarotti et al., 2024, when Φ = −1 there is complete wetting of the membrane by the condensate phase, while Φ = +1 corresponds to dewetting of the membrane by the condensate phase. The geometric factor, Φ, is negative if the membrane prefers the condensate over the exterior buffer and positive otherwise[67]. We followed the same procedure to measure θ_{in}, the intrinsic contact angle.

Fluorescence Recovery After Photobleaching

Circular bleach regions of approximate radius R = 1 µm were drawn in the center of protein droplets. Alexa-647 was imaged and bleached with a 640 nm laser. Cy3 was imaged and bleached with a 561 nm laser. Recovery curves were fit to a single exponential recovery model $f(t) = A * (1 - e^{-t/\tau})$ to calculate the recovery timescale, τ.

Passive Microrheology

Yellow–green carboxylate-modified polystyrene beads (0.5 µm diameter; FluoSpheres, Invitrogen) were used for video particle-tracking (VPT) microrheology measurements. Each sample was prepared by mixing protein and RNA to a final concentration of 40 µM protein and 300 nM viral RNA or 1 mg/mL polyrA in 150 mM NaCl, 20 mM Tris-HCl buffer, pH 7.5. Next, 50 µL of the protein and RNA sample was mixed with 1 uL of a 1:100 dilution of the fluorescent tracer bead solution and the sample was plated on a 1.5 thickness slide pre-treated with Pluronic F127. The sample was covered with a CherryTemp microfluidic temperature controller chip and the sample was set to 37 ˚C and incubated for 1 hour.

VPT measurements were conducted on a Zeiss Axio Observer 7 inverted microscope equipped with an Axiocam 702 monochrome sCMOS camera (Zeiss), employing a 63x, 1.4-numerical aperture plan-apochromatic oil-immersion objective. The microscope focus was adjusted to the midsection of the protein droplets for VPT acquisition. Epifluorescence video imaging was initiated at the 1-hour timepoint, with fluorescence excitation using a 475-nm light-emitting diode (Colibri 7, Zeiss). Videos of the tracer beads diffusing within the condensate were collected at 100 frames per second for 2,000 frames. Imaging was conducted at 37 ˚C. For each sample, three independent samples were made on different days, and ~20 videos were collected from each sample, with each video containing ~5–50 tracer beads. Viscosity data presented in Figure 4 D - G and Supplemental Figure 8 D - E are the average of these independent trials.

Data analysis was conducted using the open-source particle tracking package TrackPy (v0.5.0)[68] in Python and customized as needed. The TrackPy particle tracking code was used to analyze the collected videos, starting with extracting particle trajectories. The MSD was calculated from the trajectories of individual beads, followed by calculating the ensemble-average MSD. To remove the static error from the MSD curves for calculating viscosities, we corrected the ensemble-average MSD by subtracting the noise floor from the MSD curves[69]. In general, the ensemble-average MSD often scales as a power law with lag time τ, as given by

$$< r^2(\tau) > = 2dD\tau^{\alpha}$$

where d is the number of dimensions (here d = 2, because data collection and analysis were conducted in the x–y plane), D is the diffusion coefficient, and α is the diffusivity exponent. For a purely viscous fluid, the diffusivity exponent α is unity, and the Stokes-Einstein relation can be used to calculate the viscosity[70]. The

α values for all the condensates tested were in the range of 0.3–1.1. We therefore used the Generalized Stokes-Einstein Relation (GSER) to measure the viscoelastic properties of the condensates[70]. The frequency dependent GSER in the Fourier domain is represented by the following equation:

$$G^*(\omega) = G'(\omega) + iG''(\omega) = \frac{d\, k_B\, T}{3\pi a(i\omega) < \Delta r^2(\omega) >}$$

where G*(ω) is complex shear modulus, k_B is Boltzmann's constant, T is the temperature, a is the bead radius, G'(ω) and G" (ω) are the frequency-dependent storage (elastic) and loss (viscous) moduli, respectively , and $< \Delta r^2(\omega) >$ is the unilateral Fourier transform of the MSD. We use an algebraic approach proposed by Mason et al. to estimate the Fourier transform of the MSD, which approximates the local MSD as a power-law function[50]. The algebraic expression is given by the following equation:

$$|G^*(\omega)| = \frac{d\, k_B\, T}{3\pi a < \Delta r^2(\tau = 1/\omega) > \Gamma[1 + \alpha(\tau = 1/\omega)]}$$

$$G'(\omega) = |G^*(\omega)| \cos\left(\frac{\pi\alpha(\omega)}{2}\right)$$

$$G''(\omega) = |G^*(\omega)| \sin\left(\frac{\pi\alpha(\omega)}{2}\right)$$

where $\alpha(\tau) = d\ln\left(\Delta r^2(\tau)\right)/d\ln(\tau)$ is the local power law exponent describing the logarithmic slope of $\Delta r^2(\tau)$ at $\tau = 1/\omega$ and Γ is the Gamma function. Next, cubic spline interpolation fitting is used on the calculated G' and G" data to reduce measurement noise generated in the algebraic conversion[71]. We plot the fitted G' and G'' to identify the cross-over frequency, or the timescale at which the material transitions from an elastic-dominant to a viscous dominant regime. To extract the zero-shear viscosity from the viscoelastic moduli, we use the following equation:

$$\eta(\omega) = \frac{G''(\omega)}{\omega}$$

and obtain the limit of η(ω) at low frequencies[50]. The presented viscoelastic moduli and zero-shear viscosities are the average from multiple videos (at least n = 10) taken from 3 independent samples.

The noise floor of the 500 nm beads was measured by allowing a solution of beads in water to dry on the glass surface of a slide, resulting in beads adhered to the glass surface. We acquired the trajectories

of the beads adhered to the glass surface using the same parameters and experimental setup as used for VPT studies of the samples.

Micropipette aspiration

The micropipette aspiration experiments were carried out on a Ti2-A inverted fluorescence microscope (Nikon, Japan) equipped with a motorized stage and two motorized 4-axes micromanipulators (PatchPro-5000, Scientifica) and a multi-trap optical tweezers (Tweez305, Aresis, Slovenia) according to the protocol we reported previously[52,53]. An oil immersion objective (100X; NA 1.30; Nikon) was integrated with an objective heating collar (OKOlab) and temperature controller (OKOlab) for 37 °C measurements. Micropipettes were made by pulling glass capillaries using a pipette puller (PUL-1000, World Precision Instruments). The pipette tip was then cut to achieve an opening diameter ~5 μm. Subsequently, the pipette was bent to an angle of approximately 40° using a microforge (DMF1000, World Precision Instruments).

MPA experiments were carried out in glass-bottom dishes (ES56291, Azer Scientific, US) that were pre-treated with 5% Pluronic F-127 (P2443-250G, Sigma) for 10 minutes to prevent adhesion of condensates to the glass. The micropipette was filled with the same buffer used in microscopy experiments (150 mM NaCl, 20 mM Tris-HCl, pH 7.5) using a MICROFIL needle (World Precision Instruments). The filled micropipette was then mounted onto a micromanipulator. The rear end of the pipette was connected to an automatic pressure controller (Flow-EZ, Fluigent; Pressure resolution 1 Pa).

Optical tweezers were used to contact and merge droplets to achieve a large (> 5 μm) condensate for easier MPA measurements and analysis. A secondary micropipette was used to hold the condensate during MPA. To minimize sample evaporation, 1.5 mL Milli-Q water was added to the edge of the dish, and the dishes were covered with a thin plastic wrap with a ~2 mm hole for pipette insertion. We observed that in vitro condensates always wet the inner wall of uncoated micropipettes. Therefore, the analysis of the MPA data follows the protocol described in Roggeveen et al[53]. Briefly, normalized aspiration length (aspiration length, Lp, over the pipette radius, Rp) was segmented according to the pressure steps. For each segment, the slope of a linear fitting of $(Lp/Rp)^2$ vs. time is equal to the effective shear rate. Then, the slope of aspiration pressure vs. shear rate graph gives 4η.

Fluorescence Polarization

Fluorescence polarization measurements were performed on a Tecan Spark microplate reader in a 384-well black plate at 20°C. A monochromator set the excitation wavelength at 485 nM and the emission wavelength at 535 nm, with a 20 nm bandwidth. Purified N or pN protein was serially titrated in 150 mM NaCl, 20 mM Tris-HCl, pH 7.5 buffer and incubated with a constant 4 nM FAM-labeled RNA for 10 min at room temperature (20˚C) prior to measurement.

The data was analyzed using Matlab V2023a, with a one-site binding curve (hyperbola) fitted to the data. K_D values from three experiments were averaged and the standard deviation calculated. Data was normalized by subtracting the initial polarization value from each dataset. The one-site binding equation utilized is $mP = \frac{mP_{Max} * [N]}{K_D + [N]}$, in which mP is the observed millipolarization, mP_{MAX} is the maximum polarization, [N] is the concentration of protein (unmodified or phosphorylated).

smFRET

Single-molecule fluorescence measurements were performed as described in Cubuk et al. 2021[8] with a Picoquant MT200 instrument (Picoquant, Germany). Briefly, FRET experiments were performed by exciting the donor dye with a laser power of ~100 µW (measured at the back aperture of the objective) at 488 nm wavelength. For pulsed interleaved excitation of donor and acceptor, we used a repetition rate of 20 MHz for the donor excitation and a delay of approximately 25 ns for acceptor excitation. Acceptor excitation was achieved by using a white laser (SuperK Extreme, NKT Photonics, Denmark), filtered by a z582/15 band pass filter (Chroma). Acceptor excitation power was adjusted to match the acceptor emission intensity to that of the donor (between 50 and 70 µW). Single-molecule FRET efficiency histograms were acquired from samples with protein concentrations of 100 pM labeled protein and the population with stoichiometry corresponding to 1:1 donor:acceptor labeling was selected. Photon detection events were stored with 16 ps resolution.

Proteins were designed and prepared as described in Cubuk et al. 2021[8]. Following preparation, protein for smFRET experiments was phosphorylated using the protocol described above, with the exception of the use of 200 mM β-mercaptoethanol instead of 5 mM DTT. All samples were prepared in 50 mM HEPES pH 7.4, 150mM KCl, 200 mM β-mercaptoethanol (for photoprotection), 0.001% Tween 20 (for limiting surface adhesion) unless otherwise stated. All measurements were performed in custom-made

glass cuvettes coated with PEG. Each sample was measured for at least 30 min at room temperature (295 ± 0.5 K). Protein concentrations were (1) 100 pM labeled protein for the low concentrations or (2) 100 pM labeled protein + 1 µM unlabeled protein for high concentration for the full-length construct or (3) 100 pM labeled protein + 4 µM unlabeled protein for high concentration for N^{1-246}.

Determination of root mean square inter-dye distances from mean FRET transfer efficiencies was conducted as described in Cubuk et al. 2024[72]. Briefly, the Gaussian chain model was employed in the conversion, which relies on a single parameter, the root-mean-squared inter-dye distance $r=\langle R^2\rangle^{1/2}$. Estimates for this parameter were obtained by numerically solving: $\langle E \rangle = \int_0^\infty E(R)P(R)dR$ where <E> is the mean transfer efficiency, *R* is the inter-dye distance, *P(R)* represents the Gaussian chain distribution, and *E(R)* is the Förster equation for the dependence of transfer efficiency on distance *R* and Förster radius R_0.

Small-Angle X-ray Scattering

Small-angle X-ray scattering (SAXS) measurements were made at 16-ID-C LIXS beamline (National Synchrotron Light Source II (NSLS-II), Brookhaven National Laboratory; 15.14 keV X-rays (λ= 0.8189 Å) and two Pilatus 1 M detectors). Samples were prepared by diluting protein into 150mM NaCl, 20mM Tris-HCl buffer to the concentrations desired (0.5 mg/mL – 4 mg/mL). Data over a *q* range of 0.005–0.25 $Å^{-1}$ was analyzed. Background subtraction was done using the scattering from the storage buffer (150mM NaCl, 20mM Tris-HCl, pH 7.5) and by scaling the buffer and sample intensities at the q ~ 2 $Å^{-1}$ water peak.

The data were analyzed in BioXTAS RAW 2.1 with ATSAS 3.0.4 to determine the radius of gyration (R_g) by Guinier analysis, the compactness of the particle by Kratky plots and pair-distance distribution functions, $P(r)$. R_g from $P(r)$ was compared with the Guinier R_g to ensure internal consistency in data analyses. D_{max} was calculated from $P(r)$. Bead model reconstructions using a dummy atom model were obtained from the $P(r)$ functions generated and stored as .out files using GNOM in BioXTAS RAW 2.1 using the SAXS data as input. Bead models were generated using the DAMMIN program in the ATSAS 3.0.4 software package assuming single-phase objects.

Bibliography

1. Kim, D. *et al.* The Architecture of SARS-CoV-2 Transcriptome. *Cell* **181**, 914-921.e10 (2020).

2. McBride, R., van Zyl, M. & Fielding, B. C. The coronavirus nucleocapsid is a multifunctional protein. *Viruses* vol. 6 2991–3018 (2014).

3. Perdikari, T. M. *et al.* SARS-CoV-2 nucleocapsid protein phase-separates with RNA and with human hnRNPs. *EMBO J.* **39**, 1–15 (2020).

4. Korn, S. M., Dhamotharan, K., Jeffries, C. M. & Schlundt, A. The preference signature of the SARS-CoV-2 Nucleocapsid NTD for its 5'-genomic RNA elements. *Nat. Commun.* **14**, 1–17 (2023).

5. Roden, C. A. *et al.* Double-stranded RNA drives SARS-CoV-2 nucleocapsid protein to undergo phase separation at specific temperatures. *Nucleic Acids Res.* **50**, 8168–8192 (2022).

6. Ye, Q., West, A. M. V., Silletti, S. & Corbett, K. D. Architecture and self-assembly of the SARS-CoV-2 nucleocapsid protein. *Protein Sci.* **29**, 1890–1901 (2020).

7. Morse, M., Sefcikova, J., Rouzina, I., Beuning, P. J. & Williams, M. C. Structural domains of SARS-CoV-2 nucleocapsid protein coordinate to compact long nucleic acid substrates. *Nucleic Acids Res.* **51**, 290–303 (2023).

8. Cubuk, J. *et al.* The SARS-CoV-2 nucleocapsid protein is dynamic, disordered, and phase separates with RNA. *Nat. Commun.* **12**, 1–17 (2021).

9. Ribeiro-Filho, H. V. *et al.* Structural dynamics of SARS-CoV-2 nucleocapsid protein induced by RNA binding. *PLoS Comput. Biol.* **18**, 1–30 (2022).

10. Tung, H. Y. L. & Limtung, P. Mutations in the phosphorylation sites of SARS-CoV-2 encoded nucleocapsid protein and structure model of sequestration by protein 14-3-3. *Biochem. Biophys. Res. Commun.* **532**, 134–138 (2020).

11. Wu, C. *et al.* Characterization of SARS-CoV-2 nucleocapsid protein reveals multiple functional consequences of the C-terminal domain. *iScience* **24**, 102681 (2021).

12. Bouhaddou, M. *et al.* The Global Phosphorylation Landscape of SARS-CoV-2 Infection. *Cell* **182**, 685-712.e19 (2020).

13. Wu, C. H. *et al.* Glycogen synthase kinase-3 regulates the phosphorylation of severe acute respiratory syndrome coronavirus mucleocapsid protein and viral replication. *J. Biol. Chem.* **284**, 5229–5239 (2009).

14. Fung, T. S. & Liu, D. X. Post-translational modifications of coronavirus proteins: roles and function. **13**, 405–430 (2018).

15. Patton, D., Stohlman, S. A., Fleming, J. & Lai, A. M. C. Synthesis and Subcellular Localization of the Murine Coronavirus Nucleocapsid Protein. *Virology* **130**, 527–532 (1983).

16. Yaron, T. M. *et al.* Host protein kinases required for SARS-CoV-2 nucleocapsid phosphorylation and viral replication. *Sci. Signal.* **15**, 1–16 (2022).

17. Carlson, C. R. *et al.* Phosphoregulation of Phase Separation by the SARS-CoV-2 N Protein

Suggests a Biophysical Basis for its Dual Functions. *Mol. Cell* **80**, 1092-1103.e4 (2020).

18. Wu, C. H., Chen, P. J. & Yeh, S. H. Nucleocapsid phosphorylation and RNA helicase DDX1 recruitment enables coronavirus transition from discontinuous to continuous transcription. *Cell Host Microbe* **16**, 462–472 (2014).

19. Peng, T. Y., Lee, K. R. & Tarn, W. Y. Phosphorylation of the arginine/serine dipeptide-rich motif of the severe acute respiratory syndrome coronavirus nucleocapsid protein modulates its multimerization, translation inhibitory activity and cellular localization. *FEBS J.* **275**, 4152–4163 (2008).

20. Scherer, K. M. *et al.* SARS-CoV-2 nucleocapsid protein adheres to replication organelles before viral assembly at the Golgi/ERGIC and lysosome-mediated egress. *Sci. Adv.* **8**, (2022).

21. Wolff, G. *et al.* A molecular pore spans the double membrane of the coronavirus replication organelle. *Science (80-.).* **369**, 1395–1398 (2020).

22. Savastano, A., Ibáñez de Opakua, A., Rankovic, M. & Zweckstetter, M. Nucleocapsid protein of SARS-CoV-2 phase separates into RNA-rich polymerase-containing condensates. *Nat. Commun.* **11**, (2020).

23. Iserman, C. *et al.* Genomic RNA Elements Drive Phase Separation of the SARS-CoV-2 Nucleocapsid. *Mol. Cell* **80**, 1078-1091.e6 (2020).

24. Roden, C. A. *et al.* Double-stranded RNA drives SARS-CoV-2 nucleocapsid protein to undergo phase separation at specific temperatures. *Nucleic Acids Res.* **50**, 8168–8192 (2022).

25. Lasker, K. *et al.* The material properties of a bacterial-derived biomolecular condensate tune biological function in natural and synthetic systems. *Nat. Commun.* **13**, 5643 (2022).

26. Yamasaki, A. *et al.* Liquidity Is a Critical Determinant for Selective Autophagy of Protein Condensates. *Mol. Cell* **77**, 1163-1175.e9 (2020).

27. Kota, D. & Zhou, H.-X. Macromolecular Regulation of the Material Properties of Biomolecular Condensates. *J. Phys. Chem. Lett.* 5285–5290 (2022) doi:10.1021/acs.jpclett.2c00824.

28. Carlson, C. R. *et al.* Phosphorylation modulates liquid-liquid phase separation of the SARS-CoV-2 N protein. *bioRxiv* 1–31 (2020) doi:10.1101/2020.06.28.176248.

29. Carlson, C. R. *et al.* Reconstitution of the SARS-CoV-2 ribonucleosome provides insights into genomic RNA packaging and regulation by phosphorylation. *J. Biol. Chem.* **298**, 102560 (2022).

30. Yuan, F. *et al.* Membrane bending by protein phase separation. *Proc. Natl. Acad. Sci. U. S. A.* **118**, (2021).

31. Agudo-Canalejo, J. *et al.* Wetting regulates autophagy of phase-separated compartments and the cytosol. *Nature* **591**, 142–146 (2021).

32. Mangiarotti, A., Chen, N., Zhao, Z., Lipowsky, R. & Dimova, R. Wetting and complex remodeling of membranes by biomolecular condensates. *Nat. Commun.* **14**, 1–15 (2023).

33. Scherer, K. M. *et al. SARS-CoV-2 nucleocapsid protein adheres to replication organelles before viral assembly at the Golgi/ERGIC and lysosome-mediated egress*. *Sci. Adv* vol. 8 https://www.science.org (2022).

34. Klein, S. *et al.* SARS-CoV-2 structure and replication characterized by in situ cryo-electron tomography. *Nat. Commun.* **11**, (2020).

35. Collins, L. T. *et al.* Elucidation of SARS-Cov-2 Budding Mechanisms through Molecular Dynamics Simulations of M and E Protein Complexes. *J. Phys. Chem. Lett.* **12**, 12249–12255 (2021).

36. van Meer, G. Membrane lipids, where they are and how they behave: Sphingolipids on the move. *FASEB J.* **24**, 112–124 (2010).

37. Pramanik, S., Steinkühler, J., Dimova, R., Spatz, J. & Lipowsky, R. Binding of His-tagged fluorophores to lipid bilayers of giant vesicles. *Soft Matter* **18**, 6372–6383 (2022).

38. Verheije, M. H. *et al.* The Coronavirus Nucleocapsid Protein Is Dynamically Associated with the Replication-Transcription Complexes. *J. Virol.* **84**, 11575–11579 (2010).

39. Zimmermann, L. *et al.* SARS-CoV-2 nsp3 and nsp4 are minimal constituents of a pore spanning replication organelle. *Nat. Commun.* **14**, (2023).

40. Klatte, N., Shields, D. C. & Agoni, C. Modelling the Transitioning of SARS-CoV-2 nsp3 and nsp4 Lumenal Regions towards a More Stable State on Complex Formation. *Int. J. Mol. Sci.* **24**, (2023).

41. Hurst, K. R., Koetzner, C. A. & Masters, P. S. Characterization of a Critical Interaction between the Coronavirus Nucleocapsid Protein and Nonstructural Protein 3 of the Viral Replicase-Transcriptase Complex. *J. Virol.* **87**, 9159–9172 (2013).

42. Hurst, K. R., Ye, R., Goebel, S. J., Jayaraman, P. & Masters, P. S. An Interaction between the Nucleocapsid Protein and a Component of the Replicase-Transcriptase Complex Is Crucial for the Infectivity of Coronavirus Genomic RNA. *J. Virol.* **84**, 10276–10288 (2010).

43. Ni, X., Han, Y., Zhou, R., Zhou, Y. & Lei, J. Structural insights into ribonucleoprotein dissociation by nucleocapsid protein interacting with non-structural protein 3 in SARS-CoV-2. *Commun. Biol.* **6**, (2023).

44. Zhang, Z. *et al.* Structure of SARS-CoV-2 membrane protein essential for virus assembly. *Nat. Commun.* **13**, (2022).

45. He, R. *et al.* Characterization of protein-protein interactions between the nucleocapsid protein and membrane protein of the SARS coronavirus. *Virus Res.* **105**, 121–125 (2004).

46. Lu, S. *et al.* The SARS-CoV-2 nucleocapsid phosphoprotein forms mutually exclusive condensates with RNA and the membrane-associated M protein. *Nat. Commun.* **12**, (2021).

47. Klein, S. *et al.* SARS-CoV-2 structure and replication characterized by in situ cryo-electron tomography. *Nat. Commun.* **11**, 1–10 (2020).

48. Bergner, T. *et al.* Near-Native Visualization of SARS-CoV-2 Induced Membrane Remodeling and Virion Morphogenesis. *Viruses* **14**, 1–17 (2022).

49. Ma, W., Zheng, G., Xie, W. & Mayr, C. In vivo reconstitution finds multivalent RNA–RNA interactions as drivers of mesh-like condensates. *Elife* **10**, 1–32 (2021).

50. Mason, T. G. Estimating the viscoelastic moduli of complex fluids using the generalized Stokes-Einstein equation. *Rheol. Acta* **39**, 371–378 (2000).

51. Wang, Z., Lou, J. & Zhang, H. Essence determines phenomenon: Assaying the material properties

of biological condensates. *Journal of Biological Chemistry* vol. 298 (2022).

52. Wang, H., Kelley, F. M., Milovanovic, D., Schuster, B. S. & Shi, Z. Surface tension and viscosity of protein condensates quantified by micropipette aspiration. *Biophysical Reports* vol. 1 (2021).

53. Roggeveen, J. V., Wang, H., Shi, Z. & Stone, H. A. A calibration-free model of micropipette aspiration for measuring properties of protein condensates. *Biophys. J.* **123**, 1393–1403 (2024).

54. Lorenz, R. *et al.* ViennaRNA Package 2.0. *Algorithms Mol. Biol.* **6**, 122–128 (2011).

55. Iserman, C. *et al.* Genomic RNA Elements Drive Phase Separation of the SARS-CoV-2 Nucleocapsid. *Mol. Cell* **80**, 1078-1091.e6 (2020).

56. Demchenko, A. . Fluorescence Polarization and Rotational Mobility. in *Ultraviolet Spectroscopy of Proteins* 198–207 (Springer, 1986).

57. Cubuk, J. *et al.* The dimerization domain of SARS CoV 2 Nucleocapsid protein is partially disordered as a monomer and forms a high affinity dynamic complex. *bioRxiv* (2024).

58. Botova, M. *et al.* A specific phosphorylation-dependent conformational switch of SARS-CoV-2 nucleoprotein inhibits RNA binding. *Sci. Adv.* (2024) doi:10.1126/sciadv.aax2323.

59. Stuwe, H. *et al.* Phosphorylation in the Ser/Arg-rich region of the nucleocapsid of SARS-CoV-2 regulates phase separation by inhibiting self-association of a distant helix. *J. Biol. Chem.* **300**, 107354 (2024).

60. Liu, X. *et al.* Targeting the Coronavirus Nucleocapsid Protein through GSK-3 Inhibition. *medRxiv* 2021.02.17.21251933 (2021).

61. Vögele, J. *et al.* High-resolution structure of stem-loop 4 from the 5′-UTR of SARS-CoV-2 solved by solution state NMR. *Nucleic Acids Res.* **51**, 11318–11331 (2023).

62. Roden, C. & Gladfelter, A. S. RNA contributions to the form and function of biomolecular condensates. *Nature Reviews Molecular Cell Biology* vol. 22 183–195 (2021).

63. Alshareedah, I., Thurston, G. M. & Banerjee, P. R. Quantifying viscosity and surface tension of multicomponent protein-nucleic acid condensates. *Biophys. J.* **120**, 1161–1169 (2021).

64. Studier, F. W. Stable Expression Clones and Auto-Induction for Protein Production in E. coli. in *Methods in molecular biology (Clifton, N.J.)* vol. 1091 17–32 (2014).

65. Langdon, E. M. *et al.* mRNA structure determines specificity of a polyQ-driven phase separation. **1**, 922–927 (2018).

66. Angelova, M. I. & Dimitrov, D. S. Liposome Electro formation. 303–311 (1986).

67. Mangiarotti, A., Schmidt, K. V., Lipowsky, R. & Dimova, R. Lipid packing and cholesterol content regulate membrane wetting by biomolecular condensates. *bioRxiv* 1–31 (2024).

68. Allan, D. B., Thomas, C., Keim, N. C., van der Wel, C. M. & Verweij, R. W. soft-matter/trackpy: Trackpy. (2021).

69. McGlynn, J. A., Wu, N. & Schultz, K. M. Multiple particle tracking microrheological characterization: Fundamentals, emerging techniques and applications. *J. Appl. Phys.* **127**, (2020).

70. Furst EM, S. T. *Microrheology*. (Oxford University Press, 2017). doi:10.1093/oso/9780199655205.001.0001.

71. Tassieri, M., Evans, R. M. L., Warren, R. L., Bailey, N. J. & Cooper, J. M. Microrheology with optical tweezers: Data analysis. *New J. Phys.* **14**, (2012).

72. Cubuk, J. *et al.* The disordered N-terminal tail of SARS-CoV-2 Nucleocapsid protein forms a dynamic complex with RNA. *Nucleic Acids Res.* **52**, 2609–2624 (2024).

Figure 1

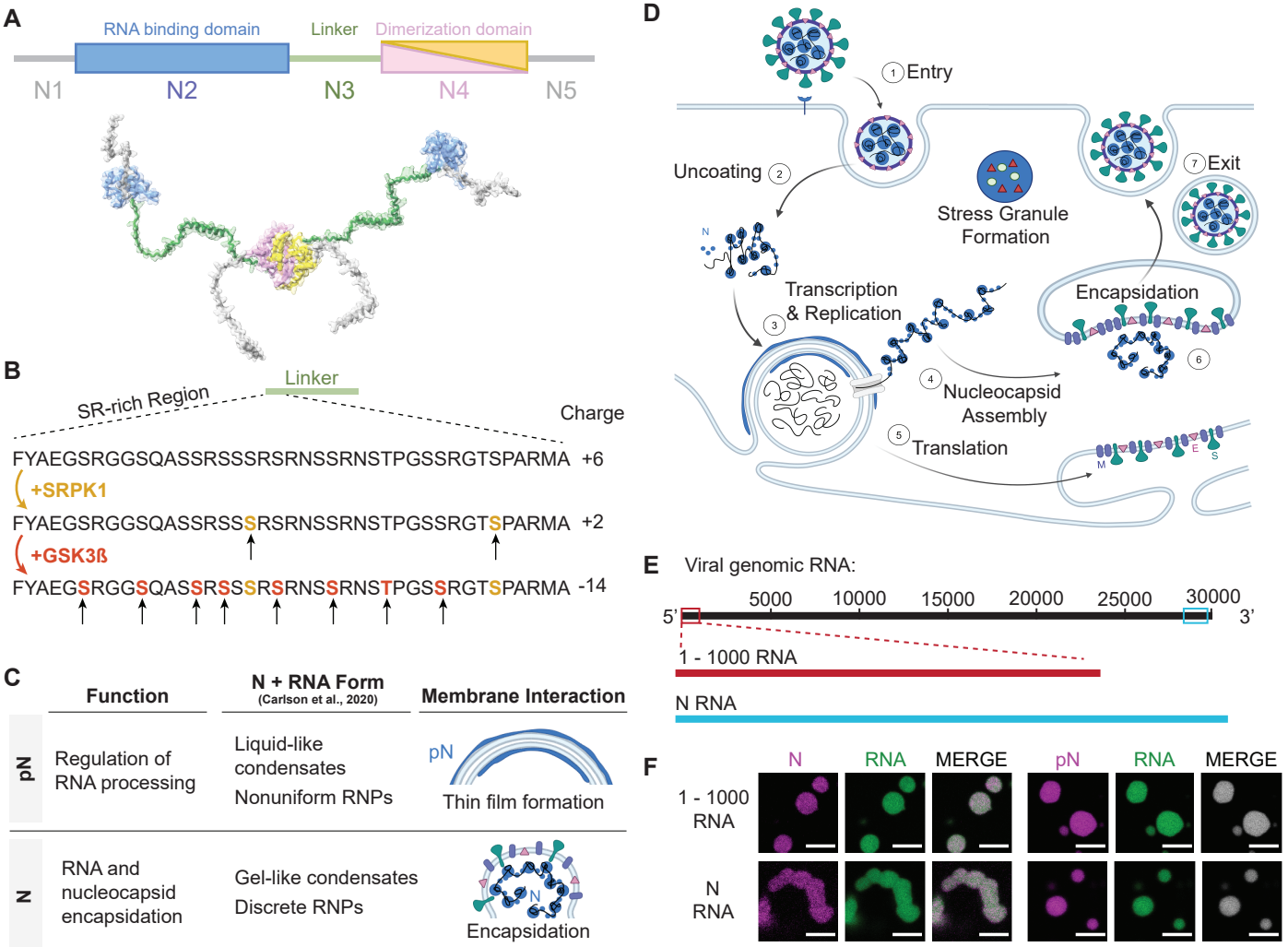
A
RNA binding domain
Linker
Dimerization domain
N1
N2
N3
N4
N5
B
SR-rich Region
Linker
Charge
FYAEGSRGGSQASSRSSSRSRNSSRNSTPGSSRGTSPARMA +6
+SRPK1
FYAEGSRGGSQASSRSSSRSRNSSRNSTPGSSRGTSPARMA +2
+GSK3ß
FYAEGSRGGSQASSRSSSRSRNSSRNSTPGSSRGTSPARMA -14
C
Function
N + RNA Form
(Carlson et al., 2020)
Membrane Interaction
pN
Regulation of RNA processing
Liquid-like condensates
Nonuniform RNPs
pN
Thin film formation
N
RNA and nucleocapsid encapsidation
Gel-like condensates
Discrete RNPs
N
Encapsidation
D
1 Entry
Uncoating 2
Stress Granule Formation
7 Exit
Transcription & Replication
3
Encapsidation
6
4 Nucleocapsid Assembly
5 Translation
M
E
S
E
Viral genomic RNA:
5000
10000
15000
20000
25000
30000
5'
3'
1 - 1000 RNA
N RNA
F
N
RNA
MERGE
pN
RNA
MERGE
1 - 1000 RNA
N RNA

Figure 2

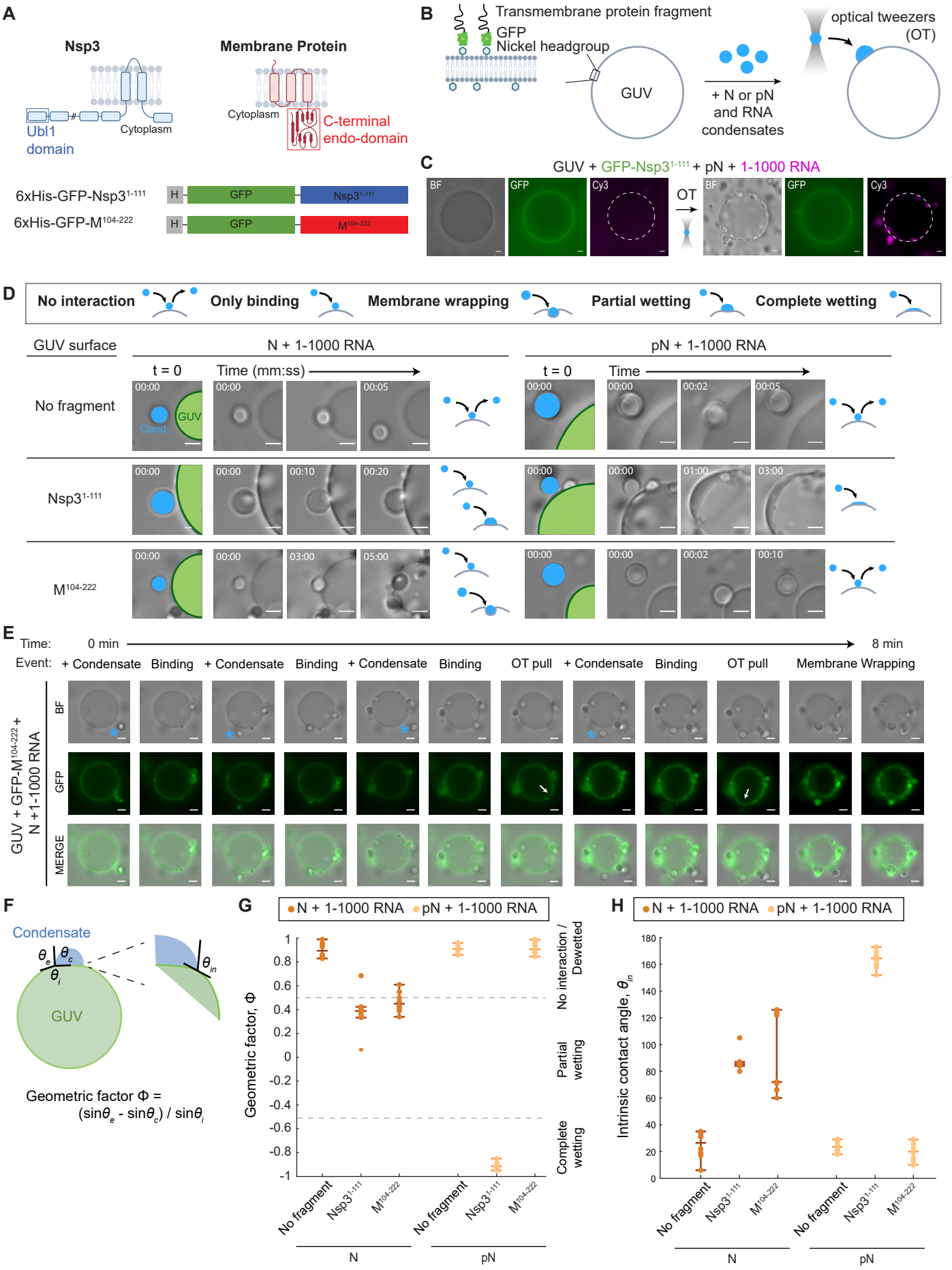
A
Nsp3
Membrane Protein
Ubl1 domain
Cytoplasm
Cytoplasm
C-terminal endo-domain
6xHis-GFP-Nsp3 1-111
6xHis-GFP-M 104-222
H
GFP
Nsp3 1-111
M 104-222
B
Transmembrane protein fragment
GFP
Nickel headgroup
GUV
+ N or pN and RNA condensates
optical tweezers (OT)
C
GUV + GFP-Nsp3 1-111 + pN + 1-1000 RNA
BF
GFP
Cy3
OT
D
No interaction
Only binding
Membrane wrapping
Partial wetting
Complete wetting
GUV surface
N + 1-1000 RNA
pN + 1-1000 RNA
t = 0
Time (mm:ss)
Time
No fragment
Nsp3 1-111
M 104-222
Cond.
GUV
E
Time:
0 min
8 min
Event:
+ Condensate
Binding
OT pull
Membrane Wrapping
GUV + GFP-M 104-222 + N +1-1000 RNA
BF
GFP
MERGE
F
Condensate
GUV
Geometric factor Φ = (sinθe - sinθc) / sinθi
G
N + 1-1000 RNA
pN + 1-1000 RNA
Geometric factor, Φ
No interaction / Dewetted
Partial wetting
Complete wetting
No fragment
Nsp3 1-111
M 104-222
N
pN
H
Intrinsic contact angle, θin

Figure 3

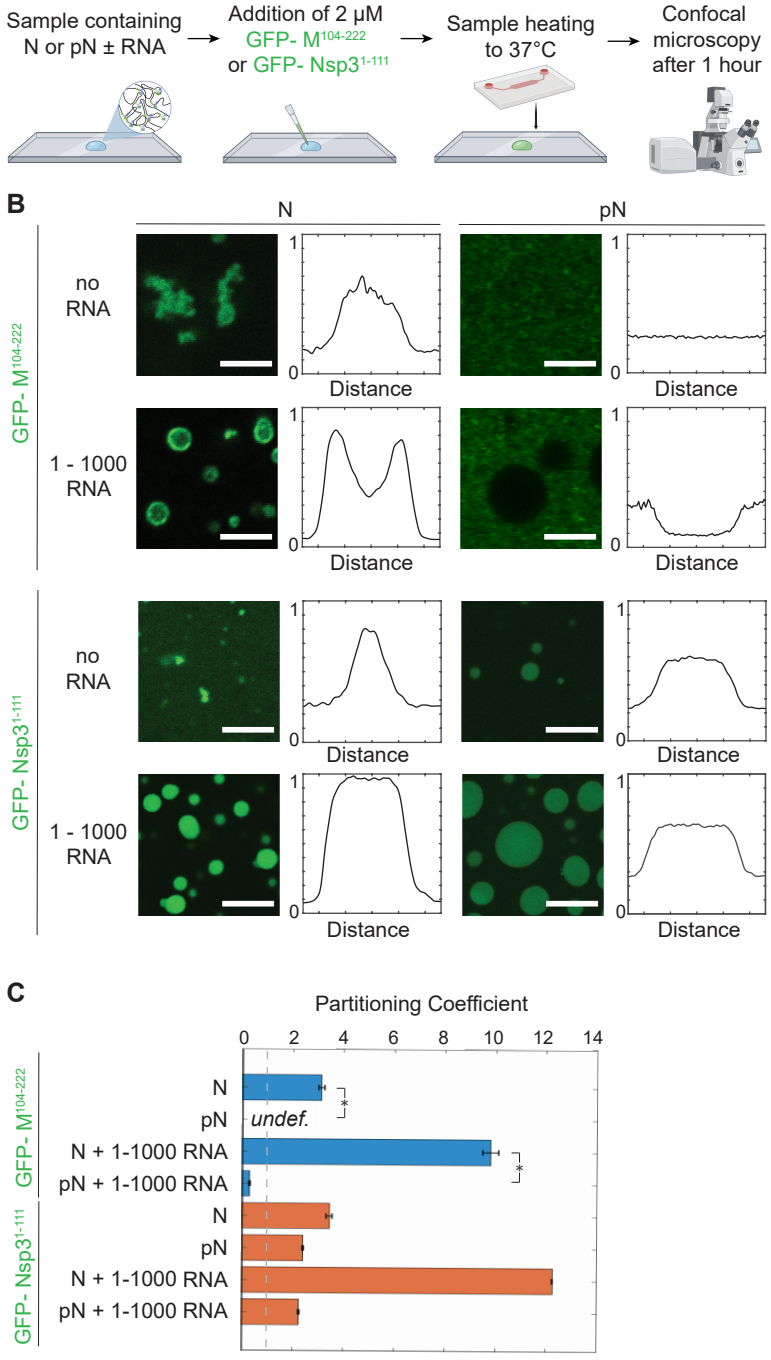
A
Sample containing N or pN ± RNA
Addition of 2 µM GFP- M104-222 or GFP- Nsp31-111
Sample heating to 37°C
Confocal microscopy after 1 hour
B
N
pN
GFP- M104-222
no RNA
1 - 1000 RNA
GFP- Nsp31-111
no RNA
1 - 1000 RNA
Distance
1
0
C
Partitioning Coefficient
0 2 4 6 8 10 12 14
GFP- M104-222
N
pN
undef.
N + 1-1000 RNA
pN + 1-1000 RNA
GFP- Nsp31-111
N
pN
N + 1-1000 RNA
pN + 1-1000 RNA
*
*

Figure 4

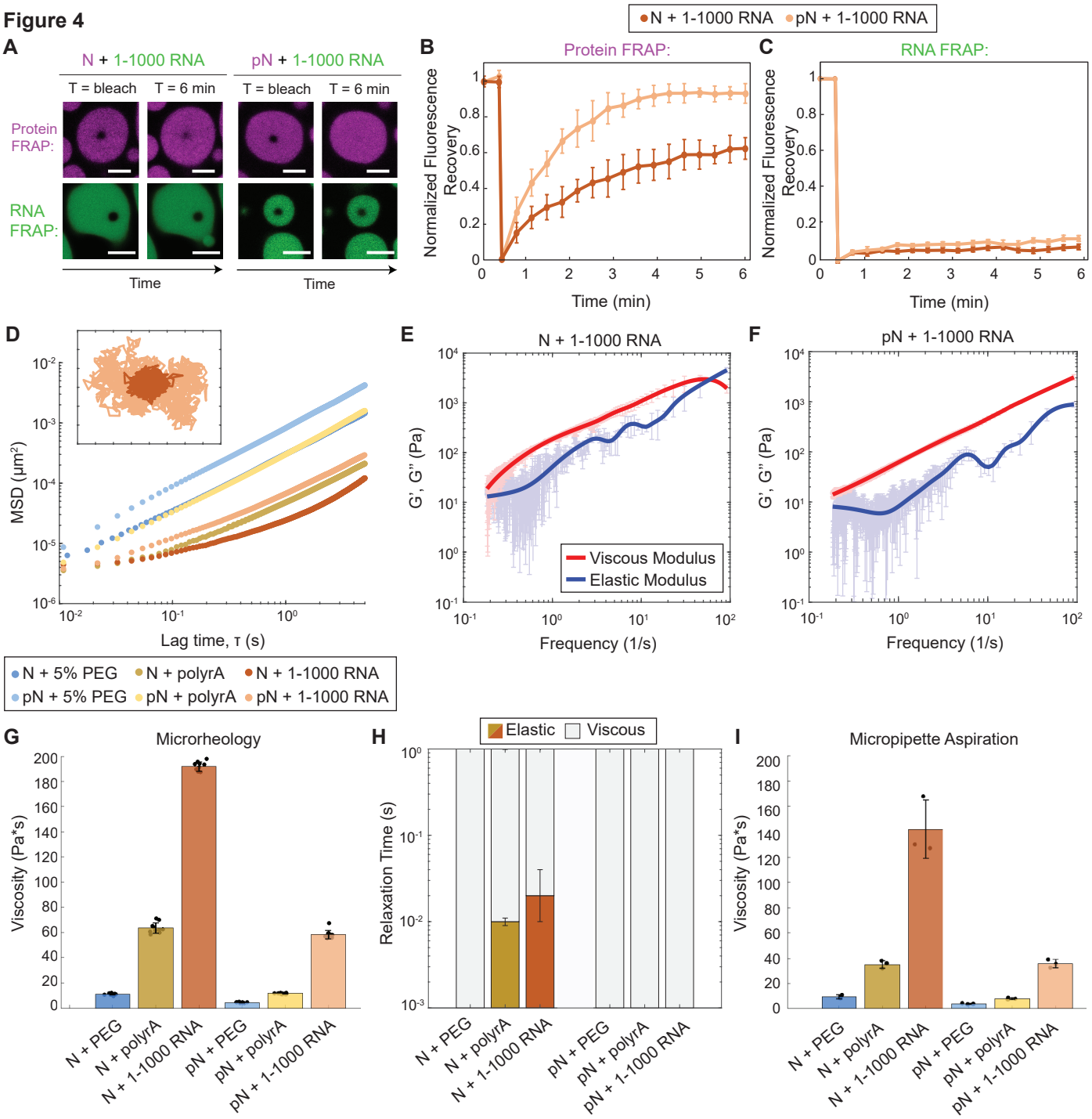
A
N + 1-1000 RNA
pN + 1-1000 RNA
T = bleach
T = 6 min
Protein FRAP:
RNA FRAP:
Time
B
Protein FRAP:
C
RNA FRAP:
N + 1-1000 RNA
pN + 1-1000 RNA
Normalized Fluorescence Recovery
Time (min)
D
MSD (μm²)
Lag time, τ (s)
E
N + 1-1000 RNA
F
pN + 1-1000 RNA
G', G'' (Pa)
Viscous Modulus
Elastic Modulus
Frequency (1/s)
N + 5% PEG
N + polyrA
N + 1-1000 RNA
pN + 5% PEG
pN + polyrA
pN + 1-1000 RNA
G
Microrheology
Viscosity (Pa*s)
H
Elastic
Viscous
Relaxation Time (s)
I
Micropipette Aspiration
N + PEG
N + polyrA
N + 1-1000 RNA
pN + PEG
pN + polyrA
pN + 1-1000 RNA

Figure 5

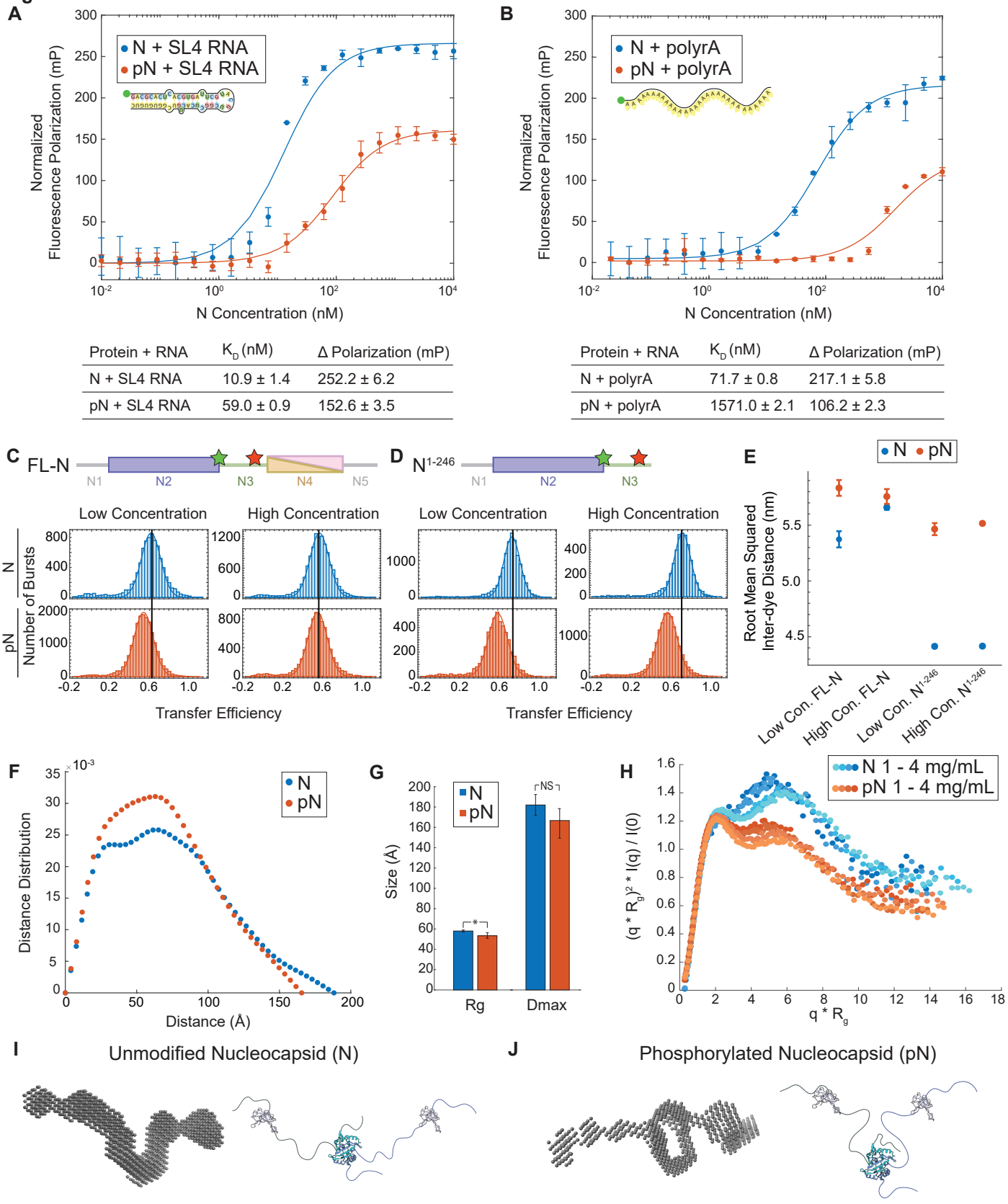

Protein + RNA	K_D (nM)	Δ Polarization (mP)
N + SL4 RNA	10.9 ± 1.4	252.2 ± 6.2
pN + SL4 RNA	59.0 ± 0.9	152.6 ± 3.5

Protein + RNA	K_D (nM)	Δ Polarization (mP)
N + polyrA	71.7 ± 0.8	217.1 ± 5.8
pN + polyrA	1571.0 ± 2.1	106.2 ± 2.3

Figure 6

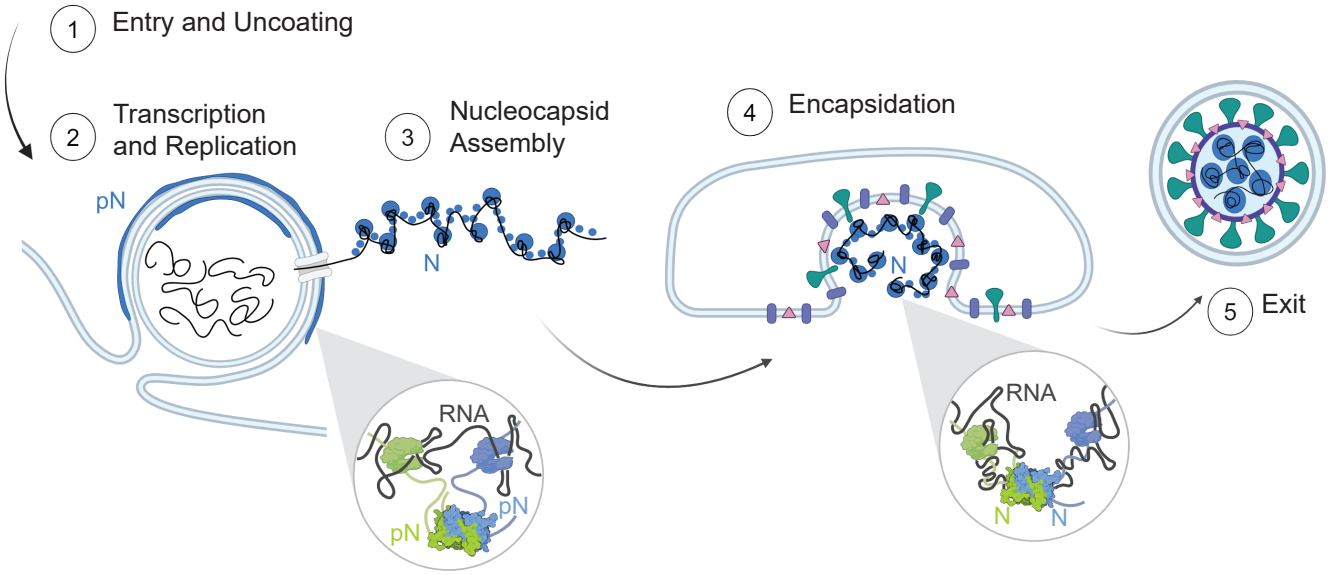
1 Entry and Uncoating
2 Transcription and Replication
3 Nucleocapsid Assembly
4 Encapsidation
5 Exit
pN
N
RNA
pN
pN
N
RNA
N
N